Measurement of the Width of the W Boson in Proton-Antiproton Collisions at $\sqrt{s} = 1.8\,TeV$

by

Jie Yang

A dissertation submitted in partial fulfillment
of the requirements for the degree of

Doctor of Philosophy

Department of Physics
New York University

May, 1995

Approved

Prof. John Sculli

To My Parents

ACKNOWLEDGEMENTS

I would first like to thank my advisor, John Sculli. Over the past several years, John has taught me a lot in physics. My gratitude to his advice and help in other respects of my life is beyond any words as well.

I would like to thank Peter Grudberg, Hiro Aihara, Natalie Roe, Ron Madaras, Darien Wood and the other members of the W/Z cross section group. Without their help, this thesis would not have been completed. My thanks also go to Geary Eppley and Bob Madden for their kindness to provide me with what I needed for my thesis analysis. I would also like to thank Peter Nemethy, Allen Mincer and Marcel Demarteau. The discussions I had with them always helped me to think deeper in physics research.

Jonathan Kotcher, Qiang Zhu, Jimmy Kourlas, Kathy Streets and other colleagues at NYU helped me a lot to get to know about the high energy physics experiments and to adapt my life to the Fermi Lab environment. I would also like to thank Haowei Xu, John Jiang, Ssumin Chang, Hailin Li, Sandor Feher, Ian Adam and many others for their friendships and many stimulating discussions about physics and life. And of course I have to thank our Fermi Lab soccer league for having made my life at Fermi Lab more enjoyable, for the excitement, the beers and the parties we had because of soccer. Oh, should I also mention that our DØ team had defeated CDF team many times in soccer field?

Last but not the least, I want to thank my mother and father. Their support and encouragement are always there for me. Their confidence and pride in me always give me strength and make me never give up.

Contents

1 Introduction **1**

1.1 Overview 1

1.2 W and Z Production 4

1.3 The W Width 8

1.4 Experiment Design 14

2 DØ Detector **16**

2.1 Central Detector 18

2.1.1 Central Drift Chamber 21

2.1.2 Forward Drift Chambers 22

2.2 Calorimeters 22

2.2.1 Central Calorimeter 28

2.2.2 End Calorimeter 28

2.2.3 Intercryostat Detectors and Massless Gaps 29

2.3 Muon Detector 29

2.4 Triggering and Data Acquisition 30

2.4.1 Level 0 30

2.4.2 Level 1 Framework 31

2.4.3 Level 2 32

3 Trigger and Event Selection **33**

3.1 Trigger 33

3.2 Event Reconstruction 35

3.2.1 Electrons and Photons 35

3.2.2 Missing $\not\!\!E_T$ and Jets 40

3.3 Event Selection 42

3.3.1 EM Energy Correction 42

3.3.2 Missing Energy Correction 42

3.3.3 The W and Z Data Sample Selection 43

4 Background **47**

4.1 Background in the W Sample 47

4.1.1 QCD Jets 47

4.1.2 $W \to \tau\nu \to e\nu\nu$ 52

4.1.3 $Z \to ee$ 54

4.1.4 $Z \to \tau\tau$ 55

4.2 Background in the Z Sample 55

4.2.1 QCD Jets 55

4.2.2 Drell-Yan Electron Pair Production 60

4.2.3 $Z \to \tau\tau$ 61

5 The Acceptance for W and Z **63**

5.1 Fiducial and Kinematic Region 64

5.2 Physics and Detector Simulation 66

5.3 Systematics Discussion 71

5.4 Comparison of the Monte Carlo with Data 74

6 Efficiency **79**

6.1 Methods 80

6.2 Efficiency for Single Electron Identification 83

6.3 Efficiency for W Events 86

6.4 Efficiency for Z Events 87

6.5 Efficiency Ratio 88

7 The W Width Measurement **90**

7.1 W and Z Cross Sections 90

7.1.1 Luminosity Determination 91

7.1.2 Cross Section Calculations 92

7.2 Extraction of the W Width 94

8 Conclusion **97**

8.1 The DØ Measured W Width 97

8.2 Future Perspectives 100

List of Figures

1.1 Leading diagrams for the production of W and Z bosons. . . . 4

1.2 Drell-Yan W and Z productions 7

1.3 The W width vs the top quark mass 13

2.1 A cutaway isometric view of the DØ Detector 18

2.2 The layout of Fermi Accelerator Facility 19

2.3 The Central Detectors 20

2.4 The cutaway view of the DØ calorimeter 26

2.5 Side view of a quarter of the Central Calorimeter and the End Calorimeter. 27

3.1 χ^2 distribution for different particles. The open histogram is for DØ Test Beam electrons, the hatched histogram is for Test Beam pions. The black dots are for electrons in a W data sample. 37

3.2 Transverse mass of the final W sample 45

3.3 Invariant mass of the final Z sample 46

4.1 The missing $\not{E}_T$ distribution. The top plot is for the signal sample, the bottom plot is for QCD background sample. . . . 50

4.2 The missing $\not{E}_T$ distribution. The dotted histograms are QCD background samples normalized in low $\not{E}_T$ regions to the signal samples which are shown in solid line. 51
4.3 P_T distribution of electrons. 53
4.4 Mass spectra for (a) di-jet events (b) γ jet events. 57
4.5 Same spectra with the fitting functions superimposed. 57
4.6 (a) The mass distribution used for input; (b) The reconstructed mass distribution. 58
4.7 (a) The mass distribution of data. (b) Fit data with Monte Carlo with $n_2 = 2.0$. The histogram is Monte Carlo. 61

5.1 Mean response to 100 GeV electrons vs TPHI3 in the vicinity of the module crack, where TPHI3 $= \Phi \times 64./2\pi$ and the crack is at $\Phi = \pi$. 65
5.2 Turn-on curves for CC electrons (a) without z correction (b) with z correction. The lines are fitted functions to the data points. 69
5.3 Turn-on curves for EC electrons (a) without z correction (b) with z correction. The lines are fitted functions to the data points. 69
5.4 For W, (a) P_T of electrons, (b) Missing $\not{E}_T$ 76
5.5 η distribution of electrons in the W events. 76
5.6 (a) W transverse mass (b) P_T of W. 77
5.7 (a) Mass of Z (b) P_T of Z. 77
5.8 P_T of leading electrons in the Z events. 78

8.1 Ratio $\Gamma(W)/\Gamma(W \rightarrow e\nu)$ as a function of top quark mass. Our data point is shown in the right window. 99

List of Tables

1.1 The vector and axial coupling constants in the partial widths calculations 11

4.1 QCD background in the W sample 52

4.2 Fitting of n_2 60

5.1 EM scale and resolution 67

5.2 Fractions of W/Z events with electrons in CC or EC 71

5.3 Systematics of Acceptance. A "-" means negligible. 72

7.1 Summary for event yields, acceptances, efficiencies and backgrounds for W and Z. 93

Chapter 1

Introduction

1.1 Overview

The interactions in nature are generally considered to be four in number: the gravitational, electromagnetic, weak and strong. Each has its own distinct characteristics and set of conservation rules. All are described by group gauge theories. Many attempts at trying to understand the interrelations among these forces have been made. The dream that the four fundamental forces are the manifestation of a simple grand unified theory is still hotly pursued by many theorists.

In the late 1960's Weinberg, Salam and Glashow (WSG) proposed a theory [1] that unified the electromagnetic and weak forces. It used the concept of spontaneous symmetry breaking in a nonabelian gauge theory and was based on the symmetry group $SU(2) \times U(1)$. The group $SU(2)$ describes the symmetry of the doublets in the weak isospin space, which are the left handed lepton families (e_L,ν_e), (μ_L,ν_μ) and (τ_L,ν_τ). The $U(1)$ group describes the symmetry

in the weak hypercharge space. A scaler field with a non-vanishing vacuum expectation value selects a preferred direction in weak isospin plus hypercharge space and thereby "spontaneously breaks" the $SU(2) \times U(1)$ symmetry. When the symmetry is broken at low energies, the electromagnetic force is transmitted by a massless photon and the weak force is transmitted by the spin 1, massive W^+, W^- and Z^0 bosons.

The first substantial evidence for the WSG theory was the observation of weak strangeness conserving neutral currents in neutrino interactions in the Gargamelle bubble chamber at CERN [2]. Then, in 1983, came the very exciting discovery of the W and Z bosons at the CERN $p\bar{p}$ collider [3]. Their measured masses and other properties were surprisingly close to those predicted by the theory.

While only the electromagnetic and weak force were successfully unified, these developments hinted at an underlying unity among all the forces. In the past few decades, much progress has been made in that direction. In particular, a new understanding of the strong force has emerged. Quantum Chromodynamics is based on the $SU(3)$ symmetry group, where $SU(3)$ is here the symmetry representation of the three-component color spin quarks, or eight massless gluons which transmit the force between the quarks. Evidence for the existence of gluons was first gathered at the e^+e^- collider PETRA. In QCD, hadrons, nuclei and their interactions can be described in terms of the quark and gluon degree of freedom. The coupling constant of the field, α_s, runs with the momentum transfer Q^2 of the process. The most important feature of QCD is asymptotic freedom [4], in which α_s vanishes logarithmically at high Q^2 (small distances) as shown clearly in [5]

$$\alpha_s(Q^2) = \frac{4\pi}{(11 - \frac{2}{3}n_f)log(Q^2/\lambda^2_{QCD})}$$

where n_f is the number of quark contributions to the vacuum polarization with $m_f^2 \leq Q^2$. The normalization parameter Λ_{QCD} can be determined by measuring experimentally the value of α_s in processes, such as the neutrino and electron scattering on nucleons at different beam energies [6]. This parameter is typically of the order 100 to 500 MeV. When the momentum transfer Q^2 is larger than this value, α_s becomes small. Hard QCD processes, characterized by short distances and high momentum transfers, can then be calculated perturbatively in terms of α_s. Therefore the calculations of hard processes can be done perturbatively, as is done in QED.

The WSG's electroweak theory, combined with this QCD theory, is called the Standard Model. It has gained popularity by having withstood many experimental tests. However, the theory is not perfect. In order to have spontaneous symmetry breaking, there must exist a Higgs particle associated with the scalar field, which has not yet been found. The origin of the masses of all fermions is still unresolved. The electroweak theory of SM is a minimal theory, meaning it has the least number of free parameters, but those free spirits do bother our theorists: they should be predicted by the theory rather than fixed by experiment. The top quark was recently discovered, completing the three families of quarks and leptons presumed by the theory. But its mass is $40 - 50$ times that of its isospin partner, for reasons unknown to the theory. The Standard Model, including QCD, leaves lots of questions unanswered and non-perturbative QCD is still at the phenomenological level. A detailed understanding of the properties of W and Z bosons will not only test the

standard theory at a higher level, but may also lead to new elements of the theory which might shed light on the theoretically unsolved problems. Several collider experiments running at the Large Electron Positron Accelerator (LEP) at CERN have studied the properties of the Z boson. The mass, width and decay properties of the Z have been measured to very high precision [7]. Precise measurements of the mass and width and other properties of the W are more difficult and very high precision has yet to be achieved.

1.2 W and Z Production

In the Standard Model, W and Z production in $p\bar{p}$ interactions is dominated by the processes shown in Figure 1.1.

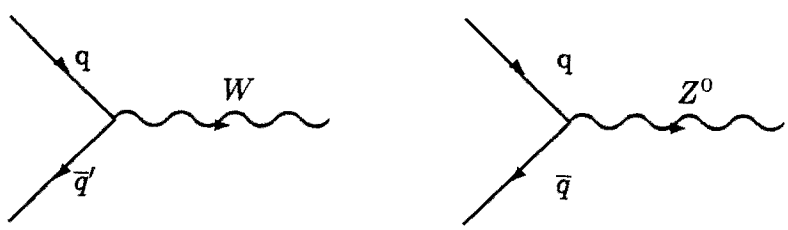

Figure 1.1: Leading diagrams for the production of W and Z bosons.

The total cross section is

$$\sigma(p\bar{p} \to W/Z + X) = \frac{1}{3}\int_0^1 dx_a \int_0^1 dx_b \sum_{qq'} q(x_a, M_W^2)\bar{q}'(x_b, M_W^2)\hat{\sigma}$$

where $x_a(x_b)$ is the momentum fraction of $q(q')$ in $p(\bar{p})$, $q(x, M_W^2)$ is the parton density function and the $\hat{\sigma}$ is the subprocess cross section.

The total production cross sections have been calculated to order α_s, and more recently to order α_s^2 in the form of K factors [8]. Most higher order corrections to W and Z production are common to both processes, making the ratio of the cross sections one of the most reliably calculated results of QCD. The only difference between higher order corrections to W and Z cross sections is that the W couples exclusively to flavour-nonsinglet channels while the Z couples to flavour-singlet channels as well; for example, two gluons can produce a Z, but not a W, via a triangle quark loop with the Z at the third vertex. This contribution vanishes, however, if up and down quark have the same mass. The ratio can be expressed as [10]

$$\frac{\hat{\sigma}(q\bar{q} \to W)}{\hat{\sigma}(q\bar{q} \to Z)} = (\text{ratios of known couplings}) + O(\alpha_s^2)[\frac{m_t^2 - m_b^2}{M_Z^2}]$$

Those $O(\alpha_s^2)$ terms have been calculated and they are less than 1% of the ratio.

The largest uncertainty then resides in the parton flux factors, or density functions, which relate the quark level processes to the $p\bar{p}$ cross sections. The flux factors for the W and Z are in the ratio

$$\frac{u\bar{d} + u\bar{d}}{u\bar{u} + d\bar{d} + s\bar{s}}$$

and depend on the relative fluxes of u,d and s quarks carried by the proton. The cross section ratio depends most significantly on the ratio of the quark

density u/d. The CTEQ [11] collaboration has recently done a comprehensive global analysis of all available data and developed new sets of parton density functions. These, together with the MRS sets [12] and GRV sets [13], provide the best fit to all the current available data from deep inelastic scattering, lepton pair production and direct photon production experiments.

We use the order α_s^2 calculations described in [8] to evaluate the cross sections predicted by the Standard Model and their ratio. For the nominal value, the CTEQ2pM pdf [11] parton density functions are used, with $M_Z = 91.19GeV$, $M_W = 80.23 \pm 0.18GeV$ [14] and $\sin^2\theta_W = 1 - M_W^2/M_Z^2 = 0.2259$.

The cross sections and their ratio at $\sqrt{s} = 1.8TeV$ are then

$$\begin{aligned}
\sigma(q\bar{q} \to W) &= 22.35nb, \\
\sigma(q\bar{q} \to Z) &= 6.708nb, \\
\frac{\sigma(q\bar{q} \to W)}{\sigma(q\bar{q} \to Z)} &= 3.33 \pm 0.03.
\end{aligned}$$

However, the W and Z are observed experimentally only through their decay products. The processes directly measured, $p\bar{p} \to W \to e\nu$ and $p\bar{p} \to Z \to ee$, are shown in the Figure 1.2. These cross sections also have been calculated to second order in α_s [8]. The measurements of these cross sections already provide a useful test of the QCD theoretical calculations.

Unlike the decay of the Z to electron and positron, which can be fully reconstructed experimentally, the W decays to one electron or positron and a neutrino, which is hard to detect because of its very small cross section with matter. The momentum of the neutrino transverse to the beam direction can be found from conservation of momentum. It is the missing transverse momentum, obtained by summing vectorially the transverse momenta of all

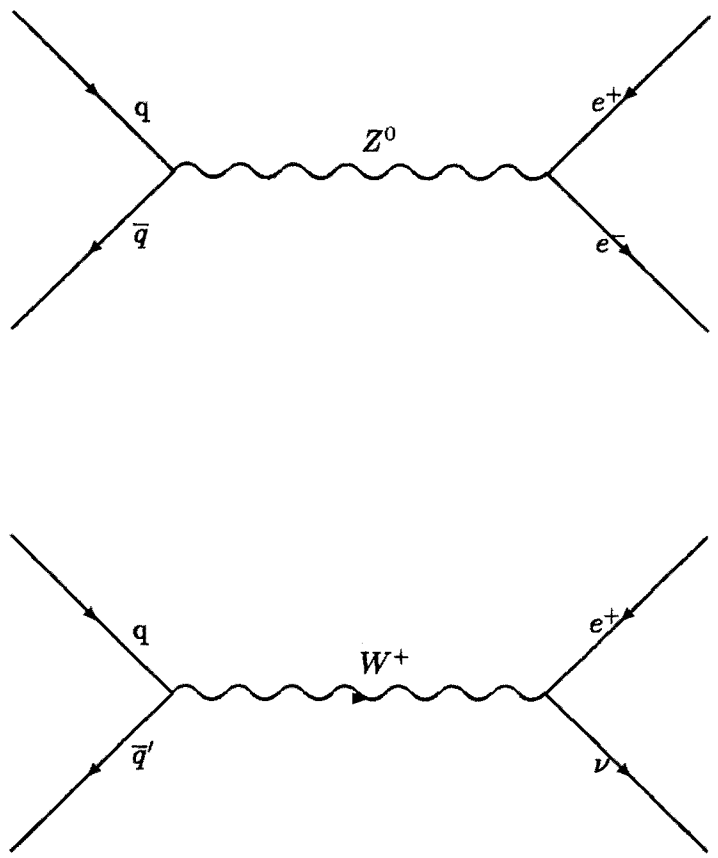

Figure 1.2: Drell-Yan W and Z productions

the particles produced in the event. The momentum along the beam direction is more difficult to obtain because much of it is carried by particles produced at small angles that escape detection. In place of the invariant mass, a variable called the transverse mass is introduced.

The usual invariant mass $m(e,\nu)$ is

$$m^2(e,\nu) = (|\mathbf{P_e}| + |\mathbf{P}_\nu|)^2 - (\mathbf{P_e} + \mathbf{P}_\nu)^2$$

where $\mathbf{P}$ is the momentum and the lepton masses are neglected. The

transverse mass is defined as

$$m_T^2(e,\nu) = (|\mathbf{p_{eT}}| + |\mathbf{p_{\nu T}}|)^2 - (\mathbf{p_{eT}} + \mathbf{p_{\nu T}})^2$$

where $\mathbf{P_T}$ now is the projection of $\mathbf{P}$ on the transverse plane.

For $W \to e\nu$ where $m(e,\nu) = M_W$,

$$0 \leq m_T(e,\nu) \leq M_W.$$

The m_T distribution [5] for a given momentum transfer squared, $\hat{s}$, assuming the W is produced at $P_T = 0$, is

$$\frac{d\hat{\sigma}}{dm_T^2} = \frac{|V_{qq'}|^2}{4\pi}(\frac{G_F M_W^2}{\sqrt{2}})^2 \frac{2 - m_T^2/\hat{s}}{[(\hat{s} - M_W^2)^2 + (\Gamma_W M_W)^2](1 - m_T^2/\hat{s})^{1/2}}.$$

The singularity at $m_T^2 = \hat{s}$ produces the so-called Jacobian Peak and the shape of the m_T distribution in the region of the peak is sensitive to both M_W and Γ_W.

1.3 The W Width

The decay widths of particles are the simplest observables. In most cases they can also be calculated with good precision.

In the Standard Electroweak Model, the relevant coupling strengths e, g, G_F, α, and the Weinberg angle θ_W, and the boson masses M_W and M_Z are related at the tree level by the equations

$$\frac{g^2}{4\pi} = \frac{e^2}{4\pi \sin^2\theta_W} = \frac{\alpha}{\sin^2\theta_W},$$

$$\frac{G_F}{\sqrt{2}} = \frac{g^2}{8M_W^2}$$

and

$$M_W/M_Z = cos^2\theta_W.$$

When the higher order corrections, such as diagrams containing loops are taken into account, these equations are no longer exactly satisfied. The choice of three fundamental parameters is required and these three parameters are used to absorb the infinite counter-terms from the higher corrections and can not be predicted from the theory. The values of the other related parameters can then be computed to the desired order in perturbation theory.

We use the on-shell renormalization scheme [15], to fix

$$\sin^2\theta_W \equiv 1 - \frac{M_W^2}{M_Z^2}$$

to all orders in perturbation theory. The muon decay constant G_F does not run with Q^2, and hence expressions using the measured gauge boson masses M_W, M_Z and G_F already contain most of the effects of the Standard Model electroweak radiative corrections.

Assuming all decaying fermions are massless compared with the masses of the W and Z, the fundamental partial widths of the W and Z, to the lowest order, are given by:

$$\Gamma(W \to l\nu) = \frac{G_F M_W^3}{6\pi\sqrt{2}}$$

and

$$\Gamma(Z \to \nu\nu) = \frac{G_F M_Z^3}{12\pi\sqrt{2}}.$$

Some recent studies [16] of these partial rates find

$$\Gamma(W \to l\nu) = \frac{G_F M_W^3}{6\pi\sqrt{2}}(1 + \delta^{SM})$$

where δ^{SM} is a very small additional radiative correction whose value is -0.35% when evaluated for a top mass of $m_t = 140GeV/c^2$ and a Higgs mass of $M_H = 100GeV/c^2$. We use $G_F = 1.16639 \times 10^{-5}GeV^{-2}$ [19] and $M_W = 80.23 \pm 0.18GeV$ [14] to calculate the partial width in Standard Model and the result is

$$\Gamma(W \to l\nu) = 0.2252 \pm 0.0015GeV$$

where the error is propagated from the W mass error.

From these partial widths, the remaining cases are derived:

$$\Gamma(W \to qq') = 3|V_{qq'}|^2\Gamma(W \to e\nu)$$

and

$$\Gamma(Z \to ll) = 8(g_V^2 + g_A^2)\Gamma(Z \to \nu\nu)$$

$$\Gamma(Z \to qq) = 24(g_V^2 + g_A^2)\Gamma(Z \to \nu\nu)$$

where the couplings are given in Table 1.1.

The ratio of the partial leptonic widths of W and Z is thus

$$\frac{\Gamma(W \to e\nu)}{\Gamma(Z \to ee)} = \frac{M_W^3}{M_Z^3}\frac{2}{1 - 4x + 8x^2}$$

where $x = sin^2\theta_W$.

It can be seen that this ratio only depends on the ratio of the boson masses M_W and M_Z. With the current experimentally measured values, this ratio can be determined with high precision.

Parton	Vector Coupling(g_V)	Axial Coupling(g_A)
ν	$+1/4$	$-1/4$
e	$-1/4 + sin^2\theta_W$	$+1/4$
u	$+1/4 - \frac{2}{3}sin^2\theta_W$	$-1/4$
d	$-1/4 + \frac{1}{3}sin^2\theta_W$	$+1/4$

Table 1.1: The vector and axial coupling constants in the partial widths calculations

The hadronic partial widths have an additional factor $(1 + \alpha_s(M_W)/\pi)$ to account for first order QCD corrections [18].

The total width is simply the sum of the individual partial widths of all possible decay modes:

$$\Gamma(W) = 3\Gamma(W \to e\nu) + 2\Gamma(W \to u\bar{d}) + 2\Gamma(W \to u\bar{s}) + \Gamma(W \to t\bar{b})$$

where $\Gamma(W \to u\bar{d}) = \Gamma(W \to c\bar{s})$, and $\Gamma(W \to u\bar{s}) = \Gamma(W \to c\bar{d})$ because all quark masses are treated to be 0 and the third generation quark mixing is neglected.

$$\Gamma(Z) = N_\nu\Gamma(Z \to \nu\nu) + 3\Gamma(Z \to ee) + 3\Gamma(Z \to d\bar{d}) + 2\Gamma(Z \to u\bar{u}).$$

where N_ν is the number of the neutrino families.

The measured total width and the leptonic partial width of the Z are known to be [19]:

$$\begin{aligned} \Gamma(Z) &= 2490. \pm 7.MeV \quad (2493 \pm 4MeV), \\ \Gamma(Z \to ee) &= 83.84 \pm 0.27MeV \quad (83.9 \pm 0.2MeV). \end{aligned}$$

where the numbers in the brackets are from the standard model predictions. The agreement with the predictions of the Standard Model is spectacular.

Focusing on the W, if the mass of the top quark is larger than the W mass, the decay $W \to t\bar{b}$ is kinematically forbidden and the total width becomes

$$\begin{aligned}\Gamma(W) &= (3 + 6(1 + \frac{\alpha_s}{\pi}))\Gamma(W \to e\nu) \\ &= 9(1 + \frac{2\alpha_s}{3\pi})\Gamma(W \to e\nu).\end{aligned}$$

The branching ratio depends only on α_s as can be seen from the above equation, and depends slightly on the V_{ij} if non-zero fermion masses are considered. The total width depends on the top quark mass. If we choose the fundamental constants as α, G_F and M_Z, a variation of m_t between 80 and 200 GeV changes the widths by about 4%, a variation of the Higgs mass M_H between 50 and 1000 GeV produces about 1% change [17]. When M_Z, M_W and G_F are chosen to be the fundamental constants, the effects are smaller because some parts are absorbed into the boson masses and G_F.

If the top mass is smaller than the W mass, allowing the decay $W \to t\bar{b}$, one has to take into account the effect of the quark masses when calculating $\Gamma(W \to t\bar{b})$. In this case, the partial decay width formula becomes [5]

$$\Gamma(W \to t\bar{b}) = 3\Gamma_W^0 |V_{tb}|^2 \lambda^{\frac{1}{2}}(1, r_t, r_b)[1 - \frac{1}{2}r_t - \frac{1}{2}r_b - \frac{1}{2}(r_t - r_b)^2]$$

where $r_t = m_t^2/M_W^2$, $r_b = m_b^2/M_W^2$ and $\lambda(a,b,c) = a^2 + b^2 + c^2 - 2ab - 2ac - 2bc$.

Sine $r_b \ll 1$, and $|V_{tb}| \cong 1$, this equation can be further simplified:

$$\Gamma(W \to t\bar{b}) = 3\Gamma_W^0[1 - \frac{3}{2}r_t + \frac{1}{2}r_t^3].$$

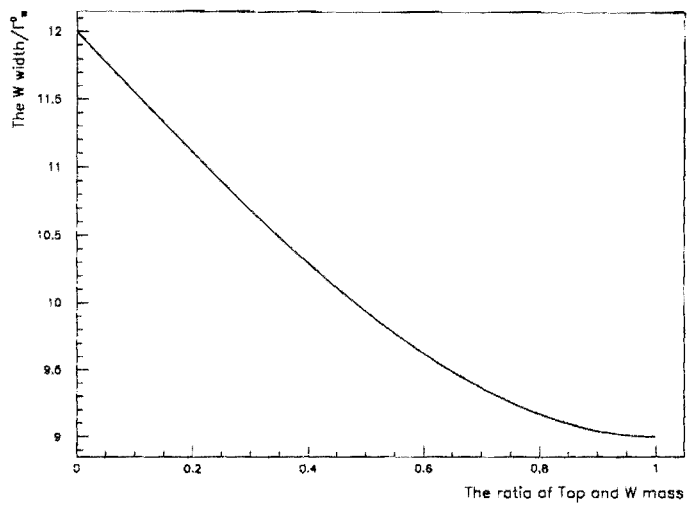

Figure 1.3: The W width vs the top quark mass

It's obvious that the total width is then sensitive to the top quark mass, as shown in Figure 1.3.

Although the DØ and CDF collaboration have announced the discovery of the top quark with a mass of $180GeV - 200GeV$ [20], they all assume the Standard Model. One nonstandard decay mode which is natural in both technicolor and supersymmetric alternatives [21] to the Standard Model is the decay,

$$t \rightarrow H^+ + b$$

of the top quark to a charged Higgs and a bottom quark. If top is heavier than the Higgs, this decay mode dominates; the present method of looking for top in final states with electrons or muons fails, and the existing bounds

disappear. Therefore the scenario of a low mass top quark has not been completely ruled out in many models, some of which are plausible extensions of the Standard Model.

1.4 Experiment Design

The difficulty in measuring directly the width of the W in $p\bar{p}$ interactions arises from the facts that the production of jets through ordinary QCD strong interaction processes overwhelms the jets produced in W production and decay. This makes the detection of the W through its hadronic decay products difficult. The relatively clean leptonic decays of the W involve an undetectable neutrino. In this case, the width can be measured through the experimentally reconstructed transverse mass, discussed in section 1.2. The shape of the transverse mass in the region of the Jacobian peak is sensitive to both W mass and width. However, the precision is compromised by the fact that the experiment energy resolutions smear the peak a lot and thus the width is strongly coupled to resolutions. An alternative method was first proposed by N. Cabbibo [22] in 1983 shortly after the discovery of W and Z bosons. The idea is to use the measurement of the cross section ratio

$$R = \frac{\sigma(p\bar{p} \to W) \cdot BR(W \to e\nu)}{\sigma(p\bar{p} \to Z) \cdot BR(Z \to ee)}$$

to get the W total width.

It's straightforward to see that this R can also be expressed as

$$R = \frac{\sigma(p\bar{p} \to W)\Gamma(W \to e\nu)\Gamma(Z)}{\sigma(p\bar{p} \to Z)\Gamma(Z \to ee)\Gamma(W)}.$$

As discussed in section 1.2, the uncertainty in $\sigma(p\bar{p} \to W)/\sigma(p\bar{p} \to Z)$ is small, as is the error in the calculated partial width $\Gamma(W \to e\nu)$, described in

section 1.3. Along with the good measurements from LEP of $\Gamma(Z)$ and $\Gamma(Z \rightarrow ee)$ or, the branching ratio $Br(Z \rightarrow ee)$, an accurate measurement of the branching ratio $Br(W \rightarrow e\nu)$, and the W width, is possible. This measurement is the principal goal of this thesis. The ratio is itself an interesting parameter that can be used to test the theory. Another advantage of this method is that it provides an inclusive measurement of the total width that is sensitive to possible unknown decay modes of W.

Chapter 2

DØ Detector

In experimental high energy physics, the particles produced in any interesting process need first to be detected by an apparatus before any resonable conclusion can be drawn about the process. Understanding of the apparatus used is thus very important for a correct interpretation of the experimental results.

The DØ Detector at the Fermilab Tevatron Collider is a large general purpose detector for the study of short-distance phenomena in high energy proton-antiproton collisions. It is approximately 13m high, 11m wide and 17m long and weighs 5500 tons. The gigantic size is dictated by the high energy and penetrating power of the produced particles and the necessity to cover most of 4π solid angle around the interaction point. The study of high mass states and high P_T phenomena are the primary goals. This includes the production of the top quark and the measurement of its mass, precision measurements of the properties of the W and Z bosons, tests of perturbative QCD, the measurement of $b-$quark production and decay, and searches for new phenomena. Electrons,

muons, jets and transverse energy imbalance relative to the beam axis are the primary objects needed to reconstruct those interesting physics processes. The DØ detector was designed and built to provide excellent identification and measurement of electrons and muons, a good measurement of parton jets at high P_T using a highly segmented calorimeter with good energy resolution, and a well controlled measure of the missing transverse energy ($\not{E}_T$) to detect the presence of neutrinos and other non-interacting particles.

A cutaway isometric view of the DØ detector is shown in Figure 2.1. The three major components of the detector are

- The Central Detector,
- The Calorimeter, and
- The Muon Detector.

These are discussed in subsequent sections of this chapter. The triggering and data acquisition system are also described here. A more general and thorough description of the whole detector system can be found in [23].

A right handed coordinate system is used at DØ. The positive z-axis is along the direction of the proton beam and the y-axis is vertically up. Azimuthal (ϕ) and polar(θ) angles are defined conventionally, with $\phi = 0$ along the positive x-axis and and $\theta = 0$ coincident with the positive z-axis. The radial distance $\rho = \sqrt{x^2 + y^2}$ is the perpendicular distance to the proton beam. The pseudo-rapidity $\eta = -log(tan(\theta/2))$, approximate the true rapidity

$$y = 1/2log((E + p_z)/(E - p_z)),$$

for finite angles of θ when a particle's mass m is small compared with its energy E.

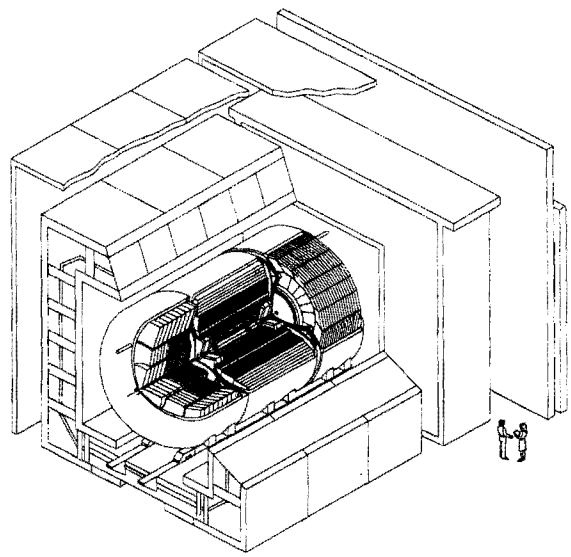

Figure 2.1: A cutaway isometric view of the DØ Detector

The location of the DØ detector at the Fermi Accelerator facility is shown in Figure 2.2. The proton and antiproton beams are focused at the interaction point DØ. They each consist of six equally spaced bunches which circle the collider every 20 μs, with the bunches crossing at $3.5\mu s$ interval. The performance of the accelerator is characterized mostly by its luminosity, defined in such a way that if σ is the $p\bar{p}$ interaction cross section, $L\sigma$ is the number of interactions per second.

2.1 Central Detector

The basic task of Central Detector (CD) is to measure the directions of charged particles. Because of the absence of a central magnetic field, the

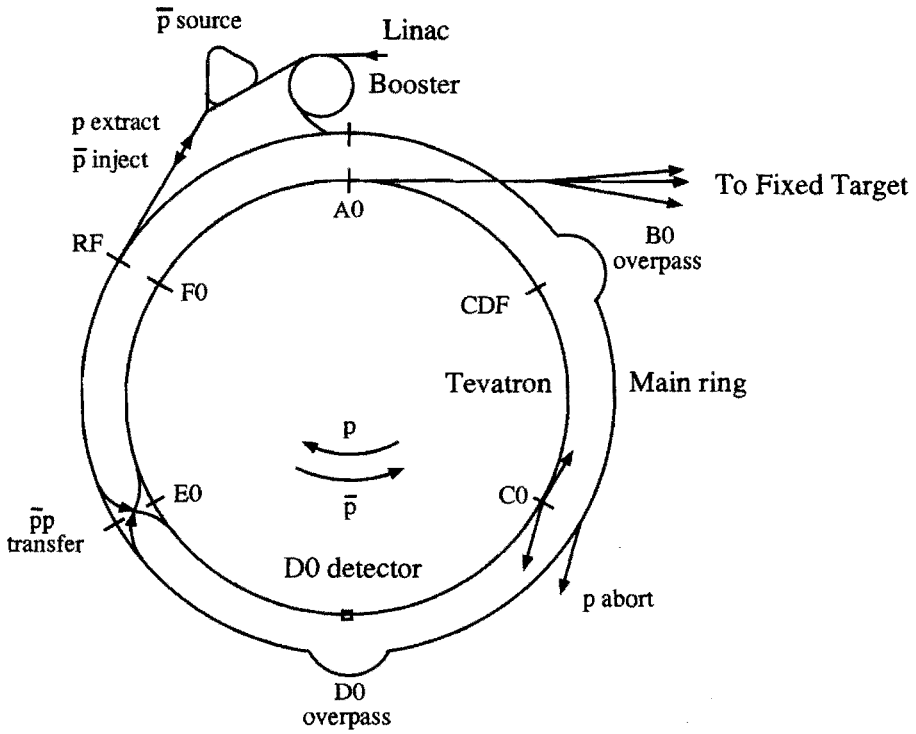

Figure 2.2: The layout of Fermi Accelerator Facility

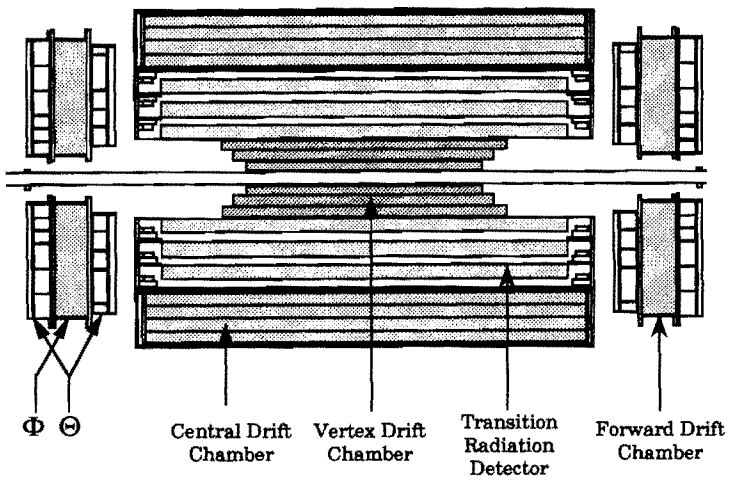

Figure 2.3: The Central Detectors

momenta of the charged particles are not measured in the tracking volume. This simplifies the requirements of the tracking chambers and allows a more compact tracking volume. Good two-track resolving power, high efficiency, and good measurement of ionization energy loss to distinguish single electrons from close-spaced conversion pairs, can then be achieved.

The CD system consists of a Vertex Drift Chamber(VTX), a Transition Radiation Detector(TRD), a Central Drift Chamber(CDC) and a Forward Drift Chamber(FDC) – as shown in Figure 2.3. The CD subsystems relevant to the measurements in this thesis are the CDC and FDC. They are all drift chambers.

Drift chamber operation, like the operation of many particle detectors, relies on the Coulomb interaction of charged particles with the medium, in this case a gas, through which the particles are passing. A charged particle interacts with the electrons in atoms of the gas molecules and creates electrons

and ions along its trajectory. These electrons and ions drift apart in the presence of an electrostatic field provided by cathode and anode wires placed in the gas, and create more ionization pairs. The anode wires (or sense wires) are very thin so that the electrostatic field becomes very large near the wires. When the electrons drift near the sense wires, they accelerate and cause more ionizations, resulting in the avalanche multiplication of electrons near the wire and measurable signals on the anodes. The arrival time of these signals is determined by the time required for the electrons created in the path of the charged particle to drift to the sense wire. The drift velocity, determined from the electric field in the gas, is then used to obtain the position of the track relative to the anode wires. The chamber is usually operated in the saturation region where the drift velocity is fairly independent of electric field intensity and the time-to-distance relationship is less complicated and more stable. Diffusion of the electrons in the gas and the direction uncertainty for the primary ion pairs limit the position resolution to around 100 μm.

2.1.1 Central Drift Chamber

The CDC provides coverage for tracks at large angles, i.e., $40^o < \theta < 140^o$, after the TRD and just prior to their entrance into the Central Calorimeter. It is a cylindrical shell of length 184 cm and radii between 49.5 cm and 74.5 cm. It consists of four concentric rings with 32 azimuthal cells per ring. In the middle of each cell, there are 7 sense wires equally spaced in radii at the same ϕ coordinate. THe wires are parallel to the z axis, and read out at one end. They provide a measurement of the position in the $r\phi$ plane, or the ϕ coordinate of a track. There are two parallel delay lines in each cell, one is

before the first sense wire and the other after the last sense wire in the cell. They propagate signals induced from the nearest neighboring sense wires. The signals are readout at the two ends and the measurement of the difference of arrival times locates the z-coordinate of a track. The $r\phi$ position resolution in the CDC is about $180\mu m$ and the z resolution is about $3mm$ for the best case.

2.1.2 Forward Drift Chambers

The FDC's extend the coverage for charged particle tracking down to $\theta \simeq 5^o$ with respect to both emerging beams. They are located at either end of the concentric barrels of the CDC, VTX and TRD and just before the entrance wall of the end calorimeters. Each FDC package consists of three separate chambers. The ϕ module has radial sense wires and measure the ϕ coordinate. It is sandwiched between a pair of θ modules whose sense wires measure the θ coordinate. The geometric composition of FDC subcells is more complicated than that of the CDC, but the operating principle is similar. The position resolution is about $200\mu m$ for $\rho\phi$ and $300\mu m$ for $r\theta$.

2.2 Calorimeters

Calorimetry is an essential part of DØ detector and also the most important part of the apparatus for the measurements in this thesis. Since there is no central magnetic field, the calorimeters must provide the energy measurement for electrons, photons and jets. In addition, they play an important role in the identification of electrons, photons, jets and muons, and in establishing the transverse energy balance in an event.

The calorimeter is basically a block of matter that intercepts the prime particle, causing it to interact. It is made thick enough to contain all the energy of the subsequent cascade or "shower" of low energy particles within its volume. Eventually all the low energy particles stop in the matter and most of the incident energy is dissipated and appears in the form of heat. Usually a small fraction of the deposited energy is detectable in the form of a more practical signals such as scintillation light or ionization charge.

Two kinds of particle showers are produced by high energy particles. Electromagnetic showers occur when the incident particle is an electron or photon, and hadronic showers are the result when the incident particle is strongly interacting.

At high energy ($E \gg 2m_e$), the interaction of electrons and photons in matter is characterized by γ emission, or bremsstrahlung, and e^+e^- pair production. These processes multiply the number of electrons and photons, the number of particles reaching a maximum when the average particle energy is approximately the critical energy, at which an electron loses the same amount of energy by radiation and ionization. Two important consequences of this multiplicative process are (i) the incident energy is linearly related to the total track length of the particles in the secondary population and (ii) the depth of the material necessary to reach the shower maximum increases only logarithmically with the energy of the incoming particle. The shower size is completely described in terms of two lengths that characterize the material of the calorimeter. The longitudinal development of the shower is largely material independent if measured in units of the radiation length X_0, while the transverse development of the shower is best described using the Moliére radius ρ. The radiation length can be expressed in terms of the nucleon number

A and the charge Z of atomic nucleus of the material [24],

$$X_0 = 180\frac{A}{Z^2}g/cm^2.$$

The Moliére radius ρ is mainly determined by the multiple scattering of the electrons when their energy reaches the critical energy value, and in terms of A and Z [24],

$$\rho \approx 7\frac{A}{Z}g/cm^2.$$

Hadronic showers are characterized by the strong interaction of incoming particle. In the process, π and K mesons are usually produced. A considerable fraction of the particle energy is ultimately transferred to nuclei. The excited nuclei release their energy by emitting first nucleons and then $\gamma's$ as they cascade to the ground state. They lose their kinetic energy through ionization. The mesons produced lose their energy by ionization or by inducing, in turn, new interactions which lead to the development of a shower. The much larger variety of interaction processes implies much larger fluctuations in the shower development compared to the pure EM shower. Therefore, the energy resolution for strongly interacting particle is worse. Since the important part of the hadronic shower is based on the nuclear interaction, the hadronic shower dimension is governed by the nuclear interaction length λ, which is related to the total hadronic cross section, which ranges between 40 and 100 mb^{-1}. The interaction length is given approximately by the formula $\lambda = 35A^{1/3}g/cm^2$ [24].

Although the shower profiles for electrons and hadrons are similar, the scale of the profiles are very different. The hadronic shower is in mean longer and broader. The differences may be used to distinguish electrons and photons from hadrons. The separation between electromagnetically interacting particles(such as electron, photon or π^0) and hadrons works best for high-Z

materials, because the ratio between λ and X_0 increases almost linearly with the Z.

For the consideration of size and cost, a sampling calorimeter is used very frequently for high energy particles. The usual configuration is a stack of many plates of dense metallic absorber, interleaved with planes of sensitive material. In these sampling calorimeters one measures the ionization loss of shower particles that traverse a sensitive layer. This is just a small fraction, usually somewhere between $1\% - 10\%$ range, but a fixed fraction of the total energy of the particle that generated the shower. This fixed fraction is called the sampling fraction and is to the first order equal to the mass ratio of the sensitive and the absorbing materials in the calorimeter.

The DØ calorimeters employ liquid argon as the sensitive layers to sample the ionization charges produced in electromagnetic or hadronic showers and a mixture of uranium and copper as the absorbing layers. The driving factor for this choice are the proven ability of liquid argon calorimeters to perform reliably and stably, the high density afforded by the combination of uranium and thin argon gaps, the radiation hardness, and the superior performance in terms of energy resolution and equalization of hadronic and electromagnetic response. Liquid argon also has property of unit gain and relatively simplicity of calibration, the flexibility in segmenting the calorimeter into transverse and longitudinal cells and the relatively low unit cost for readout electronics. However, the choice of liquid argon also brings about the complications of cryogenic systems. The DØ calorimeters consist of three components as shown in Figure 2.4: the central calorimeter (CC) and a pair of end calorimeters (ECN and ECS), each contained in a massive vessels(cryostat). There are three distinct types of modules in both CC and EC. An electromagnetic section (EM)

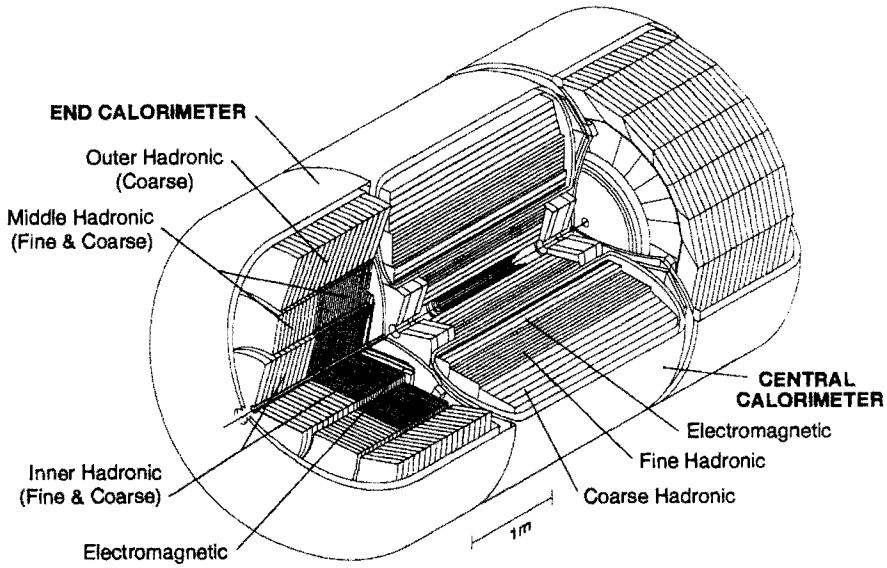

Figure 2.4: The cutaway view of the DØ calorimeter

with relatively thin uranium absorber plates to measure the energy of particle such as electron or photon which mainly interacts with the matter electromagnetically, a fine-hadronic section with thicker uranium absorber plates and a coarse-hadronic section with thick copper or stainless plates. There is a copper signal board in the middle of the liquid argon gap between two absorber plates. The electric field is established by grounding the metal absorber plates and connecting the resistive surfaces of the signal board to a positive high voltage. As the ionized electrons are collected, a signal is induced in the signal board, then grouped with other signals and transmitted through the cables to the pre-amplifier electronics.

Both CC and EC are finely segmented into pseudo-projective towers(see

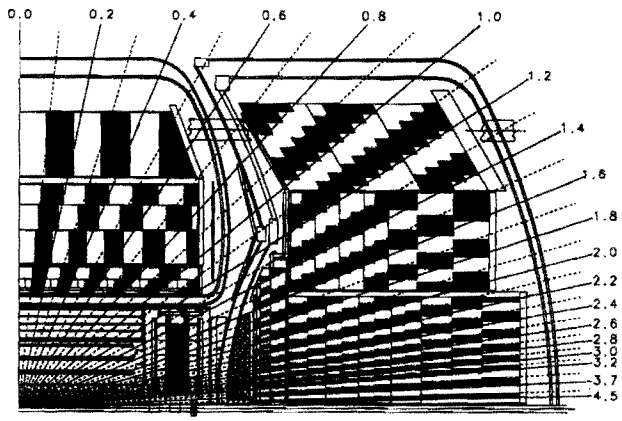

Figure 2.5: Side view of a quarter of the Central Calorimeter and the End Calorimeter.

figure 2.5) with $\delta\phi \times \delta\eta = 0.1 \times 0.1$, where ϕ is the usual azimuthal angle and η is the pseudo-rapidity. In the longitudinal direction, along the particle trajectory, the calorimeter is divided into many layers in order to provide a good measurement of the energy shower profile. In the third layer of the electromagnetic(EM) calorimeter, where the the EM shower maximum is expected, the η and ϕ segment is 0.05×0.05 instead of the normal 0.1×0.1 segment, improving the spatial resolution for electrons and photons. The electron energy resolution was well measured in a test beam at Fermilab and can be parameterized as:

$$(\frac{\sigma}{E})^2 = C^2 + (\frac{S}{\sqrt{E}})^2 + (\frac{N}{E})^2$$

where $C = 0.3\%$, $S = 15.7\%\sqrt{GeV}$, $N = 300MeV$ [23]. The response is also known to be linear with energy to better than 0.3% for electron energies

$E > 10GeV$. The DØ calorimeter also has good containment of shower energy. At $\eta = 0$, the central calorimeter has a total of 7.2 nuclear absorption lengths; at the smallest angle of the end calorimeter, the total is 10.3 nuclear absorption lengths.

2.2.1 Central Calorimeter

The CC covers roughly $|\eta| \leq 1.1$. The central calorimeter comprises of three concentric cylindrical shells. There are 32 azimuthally distributed EM modules in the inner ring, 16 fine hadronic in the surrounding ring and 16 coarse hadronic modules in the outer ring. The EM, FH and CH module boundaries are rotated so that no projective ray encounters more than one intermodule gap in order to reduce the energy loss in the cracks. The CCEM modules contain four readout sections with 2.0, 2.0, 6.8 and 9.8 radiation length (X_0). The CCFH modules contain three readout sections with 1.3, 1.0 and 0.9 interaction length λ_A. The CH contain just one depth segment of 3.2 λ_A.

2.2.2 End Calorimeter

EC extends to $|\eta| = 4$. There are two mirror-image end calorimeters (ECN and ECS). There is just one EM module and one inner hadronic module in each EC in order to avoid the dead spaces. Outside the IH and EM modules, there are concentric rings of 16 middle and outer modules. The ECEM modules contain four readout sections of 0.3, 2.6, 7.9 and 9.3 X_0. The material in front of the cryostat brings the total absorber for the first section up to about 2 X_0. The ECIH modules are cylindrical. The fine hadronic part contains four

readout sections with 1.1 λ_A for each one and the coarse part has a single readout section with 4.1 λ_A. Each of the ECMH modules has four uranium fine-hadronic sections of about 0.9 λ_A and single stainless steel coarse-hadronic section of 4.4 λ_A. The ECOH are all stainless steel coarse-hadronic modules with the absorber plates inclined at an angle of about 60° with respect to the z axis.

2.2.3 Intercryostat Detectors and Massless Gaps

The region $0.8 \leq |\eta| \leq 1.4$ contains a large amount of uninstrumental material in the form of cryostat walls, stiffening rings and module endplates. The material profile along a particle path varies with rapidity through this region. Two scintillation counter arrays are built to correct the energy deposited in the uninstrumented walls. In addition, separate single cell structure called massless gaps also are installed in both CC and EC calorimeters. One ring with the standard segmentation is mounted on the end plates of CCFH modules. Additional rings are mounted on the front plates of both ECMH and ECOH modules. These massless gaps together with ICD provide some approximation to the standard DØ sampling of EM showers.

2.3 Muon Detector

The muon detecting system consists of five separate solid-iron toroidal magnets, together with sets of proportional tube chambers to measure track coordinates down to approximately 3°. The purpose of this system is the identifications of high P_T muons produced in $p\bar{p}$ collisions and determination

of their trajectories and momenta. Since this thesis does not use muon to tag W or Z signals, this system is irrelevant and the detail can be found in [23] for interested readers.

2.4 Triggering and Data Acquisition

The DØ trigger and data acquisition systems are designed to select and record interesting physics and calibration events efficiently. The trigger has three levels of increasing sophisticated event characterization. At a typical luminosity of $L = 5 \times 10^{30} cm^{-2} s^{-1}$ the level 0 rate is about 150 KHz. The Level 1 has to reduce the rate to 200 Hz because that is the full capacity of the Level 2 computer system. Then the Level 2 software has to reduce the rate further down to 2 Hz in order to finally write interesting events to the storing hard devices.

2.4.1 Level 0

The Level 0 is a scintillator-based trigger to register the presence of inelastic collisions and serves as the luminosity monitor. It uses two hodoscopes of scintillation counters mounted on the front surfaces of the end calorimeters. Each hodoscope has an array of counters inscribed in a 45 cm radius circle to give partial coverage for the rapidity range $1.9 \leq \eta \leq 4.3$ and nearly full coverage for $2.3 \leq \eta \leq 3.9$. These counters provide time measurements and use the coincidence of the counter signals to determine the presence of inelastic collisions. The efficiency for detecting these hard collisions is measured to be about 99% by using the beam crossing clock as an unbiased check trigger.

The L0 trigger also provides the information of z-coordinate of the primary collision vertex for the higher trigger system. Although most of collisions happen at around $z = 0$, the large spread of the Tevatron vertex distribution is like a gaussian with a sigma of 30 cm and has the potential for introducing a large error in the E_T value calculation. So a position resolution of 8 cm is required for Level 1 and 3cm for level 2. The z-coordinate in Level 0 is determined from the difference in arrival time for particles hitting the two Level 0 detectors at both ends.

At high luminosity the probability to observe multiple interactions is not very small. In this case the time difference information is ambiguous and a flag is set to identify these events to the subsequent trigger levels.

2.4.2 Level 1 Framework

Level 1 is a collection of hardware trigger elements arranged in a flexible software driven architecture which allows easy modification. All Level 1 triggers operate within $3.5\mu s$ time interval between beam crossings and they must complete their work in this time and thus contribute no dead time. The Framework gathers digital information from each of the specific Level 1 trigger devices and choose whether a particular event is to be kept for further examination. The selection of trigger is performed with a 2-dimensional AND-OR Network. 256 latched bits called AND-OR Input Terms which bear specific pieces of detector information such as one calorimeter cluster over 10 Gev, form one set of inputs to the AND-OR network. The 32 orthogonal AND-OR lines corresponding to 32 specific Level 1 triggers are the outputs of the AND-OR Network. Each of these triggers is defined by a pattern indicating,

for every AND-OR Input Terms, whether that term is required to be asserted, negated or is to be ignored. Satisfaction of one or more specific triggers results in a request for readout of full event data by the data acquisition hardware if free from front-end busy restrictions or other vetos.

The interesting Level 1 trigger device for this thesis is the Level 1 calorimeter trigger. The system operates on the analog trigger pickoffs from the calorimeter signal shaping and processing electronics and the energy signals are summed into $\delta\eta = \delta\phi = 0.2$ trigger towers out to $\eta = 4$ for both EM and Hadronic sections. It uses the z-vertex information provided by the Level 0 and several fast lookup memories to calculate the EM and hadronic transverse energies and their x and y components for each trigger tower above a fixed cut.

2.4.3 Level 2

Candidates from Level 1 are passed through the Standard DØ data acquisition pathways to a farm of microprocessors which serve as event builders as well as the Level 2 trigger systems. Sophisticated algorithms reside in the Level 2 processors which reduce the rate to 2Hz before passing them on to the Host computer for event monitoring and recording on tapes. There are 50 software event-filtering nodes. The VAXELN filtering process in each node is built around a series of filter tools. Each tool has a specific function related to identification of a type of particle or event characteristic. The interesting ones for this thesis are those for jets, calorimeter EM cluster and missing $\not{E}_T$. The final passed events are recorded in 8mm tapes and are presented for further detailed reconstruction for analysis.

Chapter 3

Trigger and Event Selection

The data for this analysis was collected in the first collider run of DØ starting in April, 1992 and ending in June, 1993. During this run, about $15. \pm 2. pb^{-1}$ of data was recorded on tapes.

3.1 Trigger

The final states of the process $p\bar{p} \rightarrow W \rightarrow e\nu$ and $p\bar{p} \rightarrow Z \rightarrow ee$ have at least one electron with large transverse energy. This electron naturally becomes the object to be used as a trigger for writing an event out to hardware data storing devices such as magnetic tapes.

Both W and Z events for this analysis were triggered by one single electron trigger. The level 1 requirement of this trigger was termed as EM_1_MAX or EM_1_MED. The EM_1_MAX, which was changed to the name EM_1_MED after some early data runs, demanded that there be at least one electromagnetic trigger tower whose transverse energy had to be greater than 10 GeV,

or 12 GeV for a small fraction of the early data. A trigger tower consisted of four fixed calorimeter towers, and covered 0.2×0.2 in η, ϕ space. This coverage was large enough to contain most of the EM shower energies in most cases. The level 2 requirement of the single electron trigger was a software filter called ELE_HIGH. This filter first found the highest energy readout tower ($\delta\eta \times \delta\phi = 0.1 \times 0.1$) and then used 3×3 towers centered at it to form a cluster for the Level 2 evaluations. The transverse energy was calculated for this cluster and was required to be greater than 20 GeV. Several simple parameters were quickly calculated. Cuts on these parameters had been tuned by the good electrons during the DØ test beam run and they were used to roughly match the longitudinal and transverse profiles of the energy shower in the cluster to those expected from electrons. In order to further reduce the trigger rate which was mostly restricted by the speed of writing an event to a tape, an isolation cut was added which was defined as

$$f_{iso} = \frac{E_{total}(R_{iso}) - E_{EM}(R_{core})}{E_{EM}(R_{core})} < 0.15.$$

where E_{total} was the total energy in a cone of radius $R_{iso} = 0.4$ or 0.6 and $E_{EM}(R_{core})$ was the EM energy in a cone of radius $R_{core} = 0.2$, and $R = \sqrt{\delta\phi^2 + \delta\eta^2}$. This cut was based on the fact that an electron decayed from a W or Z is typically well isolated. The similar cut will be used for final event selection as well and it will be discussed in more detail in the next section.

All events which have passed the trigger are recorded on tapes and are reconstructed by a more sophisticated program.

3.2 Event Reconstruction

The full reconstruction for a DØ recorded event is first done by the standard DØ software package DØRECO. For this thesis, all data are reconstructed by the DØRECO package version 11.

The program uses available informations from different detector components and reconstructs vertices, the candidates for electrons/photons, missing transverse energy, jets and muons for each event.

A vertex is reconstructed by using the CDC and FDC tracking information. All the reconstructed tracks in the CDC or FDC are extended to the beam axis and then z positions of these tracks are obtained. From the distributions of z a fit can be made and a vertex is thus determined.

3.2.1 Electrons and Photons

The electrons and photons are primarily identified by the calorimeters. The tracking system provides the tracking information for the further discrimination between electrons and photons.

As described in section 2.2, both electrons and photons with high energies develop similar electromagnetic showers in the calorimeters. The recorded calorimeter data is in the form of the charges collected by each calorimeter cell. The standard DØRECO package first converts the charges into energies by using the calorimeter calibration informations. Then the sum of energies in all cells in a $\delta\eta = 0.1$ by $\delta\phi = 0.1$ tower is performed. The energies in all layers of EM calorimeters and the first layer of the fine hadronic calorimeter are also summed and this sum is called an EM energy tower. A "nearest neighbor" cluster finding algorithm is employed to find the EM energy clusters associated

with electrons or photons. The concept of the algorithm is the local clustering with equivalence relations [25]. It loops all EM energy towers with transverse energy greater than 50 MeV. For each tower it finds the nearest-neighbor tower with the highest transverse energy. If such a nearest-neighbor tower is found, a local connection is made between those two towers. After all towers are looped over, towers which have connections are connected together and they are formed as clusters. The transverse energy of the formed cluster is then calculated and required to be greater than 1.5 Gev in order to be saved for the further analysis. The energy in the EM portion of the calorimeter is also required to exceed 90% of the total energy of the cluster and the energy outside the central tower must be less than 60%. Both of these requirements are designated to select clusters corresponding to narrow EM particle showers. The clusters which have passed the above cuts are the candidates for the electrons and photons.

The cross sections of QCD processes such as two jets production are about the order of 10^{-3} barns and are much more larger than W/Z's cross sections at nanobarns. Hadronic showers from QCD jets can fluctuate to look like EM showers from electrons or photons. The overall effect is that a large QCD background is still left in the data sample. Therefore several other variables are developed to be used to reduce the huge background and clean the electron/photon selections. Those variables are isolation parameter, shower shape χ^2, track match significance. They are all calculated in the DØRECO package.

The isolation variable is very useful to discriminate the QCD background because the electron from W or Z is mostly isolated, which means there are not many other particles in the vicinity of an electron or photon. A jet, however,

is composed of many collimated particles which are close to each other. So the isolation parameter for a cluster is defined as the percentage of cluster energy in the vicinity of the core towers of that cluster,

$$f_{iso} = \frac{E_{total}(R = 0.4) - E_{EM}(R = 0.2)}{E_{EM}(R = 0.2)}$$

where E_{total} is the total energy in a cone with a radius 0.4 and E_{EM} is the energy in EM section in a cone with a radius 0.2. For isolated electrons, this variable is normally small.

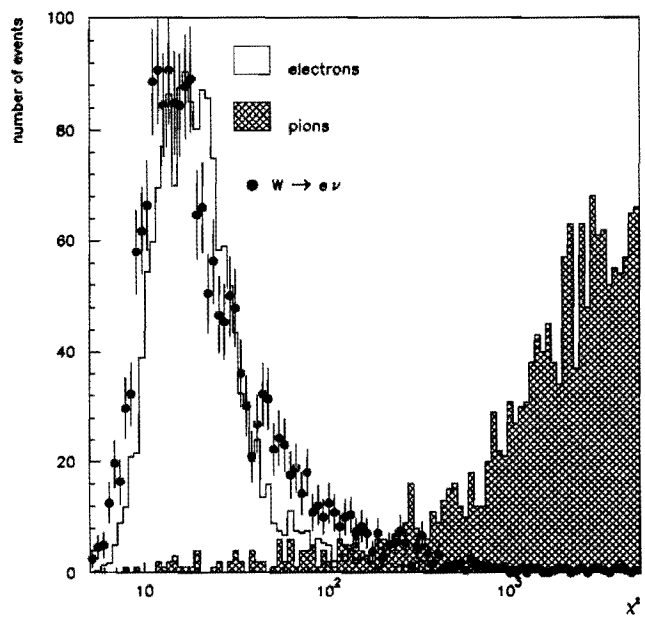

Figure 3.1: χ^2 distribution for different particles. The open histogram is for DØ Test Beam electrons, the hatched histogram is for Test Beam pions. The black dots are for electrons in a W data sample.

The shower development of electron or photons in calorimeters is also characteristically different from that of QCD generated EM like showers. The pro-

file of the shower both in longitudinal and transverse direction can be thus used to discriminate some QCD background from the signals. A covariance matrix is constructed to compare the shape of the experimentally observed shower with the expected shape of electrons or photons. In this way it also takes into account the correlations among energy deposits in the calorimeter cells.

For a sample of N electrons a covariance matrix is defined as

$$M_{ij} = \frac{1}{N}\sum_{n=1}^{N}(x_{ni} - < x_i >)(x_{nj} - < x_j >)$$

where x_i is the value of the ith observable and $< x_i >$ is the average of that observable in that sample. This matrix is of 41-dimensional because 41 variables are used to build it. The fraction of shower energy in EM layers 1, 2 and 4 are the first 3 observables. For the third EM layer where a EM shower usually is at its maximum development and the detector is more finely segmented, the fraction of shower energy in each cell in a 6×6 array centered at the hottest tower is used. These 36 observables characterize the transverse development of the shower. Finally the logarithm of the shower energy and the z position of the event vertex are included to parameterize the energy and the particle incidence angle dependence of the matrix. The matrix is tuned with Monte Carlo data. For each of the 37 detector towers at different values of η, a matrix is built from Monte Carlo electrons.

A H-matrix is then defined as $H = M^{-1}$. For an experimentally observed shower,

$$\chi^2 = \sum_{ij}(x_i - < x_i >)H_{ij}(x_j - < x_j >).$$

where x_i is the measured value of the ith observable and $< x_i >$ and

H_{ij} can be obtained from lookup tables which are calculate by tuning of H matrix. Figure 3.1 shows the distribution of χ^2 for showers from test beam electrons and pions with an energy of 25 GeV. The two distributions are clearly separated. Note that the covariance parameter χ^2 does not necessarily follow a usual χ^2 distribution, because in general the observables defining the matrix are not normally distributed, an example being the energy deposited in the layers due to the exponential nature of longitudinal shower development [26].

From the above discussion, it is obvious that a particle cluster should be rejected as an EM cluster if the χ^2 is too large.

Track information is used to distinguish electrons from photons, because only charged particles can ionize in the gas chambers through coulomb interactions and leave tracks. In DØRECO package a reconstructed track is required to be inside a 0.1×0.1 cone centered at the EM shower centroid. If this requirement is satisfied, it is categorized as an electron candidate and stored in data banks called PELC, otherwise it is saved as a photon candidate in PPHO data banks. The shower track significance is used to test the quality of match of the track with the shower centroid and is defined as

$$\sigma_{trk} = \sqrt{(\frac{\delta z}{\sigma_z})^2 + (\frac{\delta \phi}{\sigma_\phi})^2}$$

in the CDC and

$$\sigma_{trk} = \sqrt{(\frac{\delta \rho}{\sigma_\rho})^2 + (\frac{\delta \phi}{\sigma_\phi})^2}$$

in the FDC. where z, ρ and ϕ are cylindrical coordinates and all the differences δ's are calculated between the coordinates of the track and the shower centroid at the calorimeter EM layer 3. The σ's in the denominators are the

resolutions of measurement of the corresponding parameters. For good electrons with good track, σ_{trk} should be small.

All those calculated variables will be used to cut the data. The different cut values usually define the different quality of the electron or photon thus selected.

3.2.2 Missing $\not\!\!E_T$ and Jets

The missing $\not\!\!E_T$ is the only way to extract information for the escaping neutrinos. It is defined as

$$\not\!\!E_T = \sqrt{(\not\!\!E_T^x)^2 + (\not\!\!E_T^y)^2}$$

where

$$\not\!\!E_T^x = -\sum_i E_i \sin\theta_i \cos\phi_i,$$

$$\not\!\!E_T^y = -\sum_i E_i \sin\theta_i \sin\phi_i$$

where i runs over all calorimeter cells with readout signal amplitude outside a 2σ window centered on the mean of the channel noise, and E_i is the energy deposited in the ith cell with θ_i and ϕ_i as the polar and azimuthal angle of that cell respectively. For a better measurement of the missing $\not\!\!E_T$, all ICD and massless gaps are included in the summed cells.

The resolution of the missing $\not\!\!E_T$ is affected by many factors, such as energy fluctuation in the calorimeters, energy lost in and around the beam pipe and to cracks in the calorimeter, signal fluctuations caused by the uranium radioactivity , random and coherent electronic noise, etc. Studies are performed on the collider data to understand the missing $\not\!\!E_T$ resolution. Since

the missing $\not{E}_T$ is a global parameter involved the whole calorimeter, a global quantity called the scalar $\tilde{E}_T$ which is defined as

$$\tilde{E}_T = \sum_i E_i \sin\theta_i$$

is used to parameterize the resolution. It is found that the resolution can be parameterized as

$$\sigma_{\not{E}_T} = a + b \cdot \tilde{E}_T$$

where $a = 1.9$ and $b = 0.007$ for some jet events [27].

The quarks and gluons produced in a hard scattering are fragmented into collimated jets of hadrons. The number and kinematic properties of the jets are somewhat dependent on how a jet is defined in experiment. For our analysis, jets are only used to correct missing $\not{E}_T$. So we briefly describe how a jet is reconstructed.

DØ uses a cone algorithm [28] to reconstruct jets. First from an E_T ordered list of hadronic towers, preclusters are formed of contiguous towers out to a radius of about $R = 0.3$ in η and ϕ space. The preclusters are used to cut down the number of towers which are to be used as a starting point for jet formation. The precluster center in η, ϕ space is used as the starting cone center. A new E_T weighted center is then formed from all towers within a radius of $R = 0.7$ of the center. This process is repeated until the center is stable. Once the jet is formed, the E_T is required to be greater than 8 GeV to be saved, otherwise it is dropped.

Because of the difference in EM and HAD response of calorimeter, as mentioned in chapter 2, the jet energy has to be corrected. The DØRECO package only reconstructs the jets and leaves the task of energy calibration to the final phase of a different physics analysis. This will be discussed in next section.

3.3 Event Selection

After the events pass the DØ RECO analysis package, before the final selection for W and Z samples is made, several other important corrections are made to the data.

3.3.1 EM Energy Correction

The first correction to be made is the EM energy scale correction. The absolute energy scale of DØ calorimeter is provided initially by test beam energy calibration. Several modules were calibrated using beams of electrons and pions. Then the measured relationship between the electron beam momentum and electronics readout was used to set the EM scale. Using this scale calibration, the measured Z mass was found to be a few percent lower than that measured by the LEP experiment. Extensive studies were conducted. From the studies, the few percent deficit was found to be mostly multiplicative, which meant the offset of the correction was close to zero [29]. Based on this, we find the multiplicators for electrons in the central calorimeter and both end calorimeters to make the reconstructed mass of Z agree with the LEP measured value. The multiplicators are 1.072 ± 0.002 for CC electrons, 1.025 ± 0.005 for north EC electrons and 1.012 ± 0.007 for south EC electrons [30]. These multiplicators are then used to correct EM energy.

3.3.2 Missing Energy Correction

The missing $\not{E}_T$ is also corrected after the EM energy scale is corrected. The EM energy correction is stored as a vector and it is then added to the

missing $\not{E}_T$ to reconstruct a new missing $\not{E}_T$ vector.

For high P_T jet, the jet energy is corrected by scaling hadronic energy scale to em energy scale. And like after the EM scale correction, the missing Et is corrected correspondingly.

3.3.3 The W and Z Data Sample Selection

The data with run number 55217 or greater are used, bad runs are excluded. Data with run number less than 55217 are discarded because the Level 1 trigger is inefficient and it is only a small fraction (about 7% of all data). At least one vertex has to be found in an event.

Both W and Z selection requires one "tight" electron with $P_T > 25GeV$. The "tight" electron is defined as an electron

- Having passed ELE_HIGH trigger;
- Being in good fiducial regions: $|\eta| < 1.1$ and 0.01 radian in ϕ away from the EM module boundaries if a CC electron, and $1.5 < |\eta| < 2.5$ if an EC electron;
- Having EM fraction: $f_{EM} = \frac{E_{EM}}{E_{total}} > 0.95$;
- Having H-matrix $\chi^2 < 100$;
- Having Isolation: $f_{iso} < 0.10$;
- Having Track match significance: $\sigma_{trk} < 5$ if a CC electron and $\sigma_{trk} < 10$ if an EC electron.

For W, the missing $\not{E}_T$ has to be greater than 25 GeV. Events with two or more tight electrons are removed. 10338 candidate W events are found after all those requirement.

For Z, the additional requirement is that there must be a second "loose" electron with $P_T > 25GeV$. The loose electron uses the same selection cuts described above except the trigger and tracking requirement. The trigger requirement is dropped because the "tight" electron has to pass the trigger. The condition of a good track match is eliminated so that an EM cluster from either PELC or PPHO data banks can be used in order to increase the statistics of the Z sample. In addition, the invariant mass of the two electrons must be inside a mass window $75-105GeV$. 775 candidate Z events are found.

The transverse mass of W events and the invariant mass of Z events are shown in Figure 3.2 and Figure 3.3.

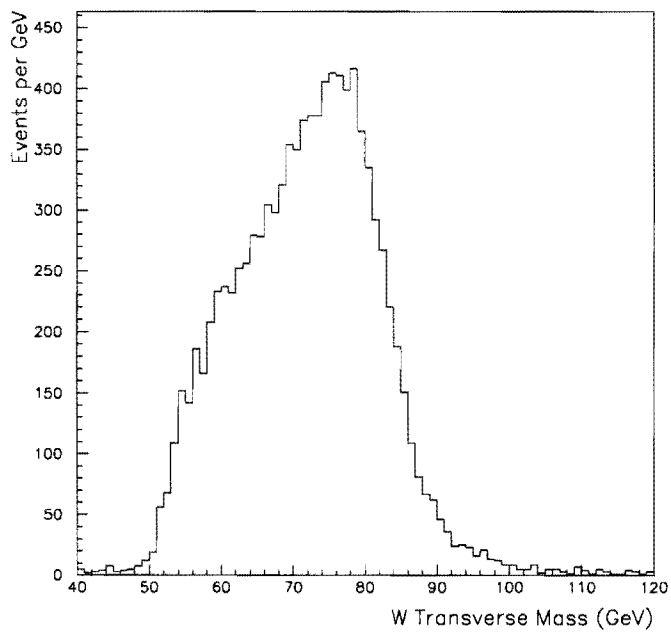

Figure 3.2: Transverse mass of the final W sample

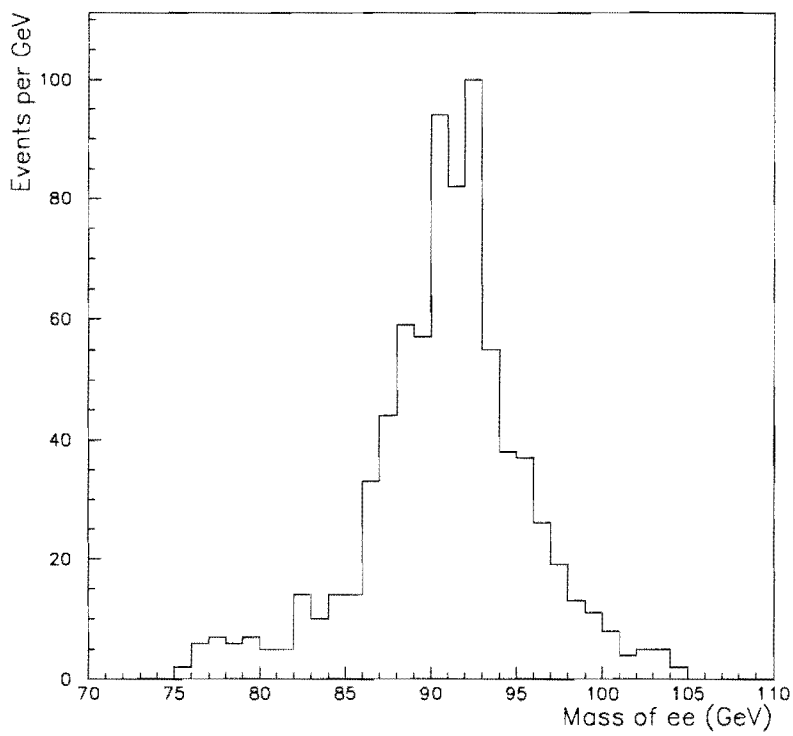

Figure 3.3: Invariant mass of the final Z sample

Chapter 4

Background

Our selection cuts have effectively reduced QCD background in our final W or Z data sample, but there is still residual QCD background left. Some physical processes produce the same event outcome as our signals. Correct estimate of these backgrounds is still needed and very important for the precision measurements.

4.1 Background in the W Sample

For the $W \rightarrow e\nu$ signals, four kinds of background are considered here. They are QCD jets production, $W \rightarrow \tau\nu$ and τ subsequently decays to $e\nu\nu$, $Z \rightarrow ee$ and $Z \rightarrow \tau\tau$.

4.1.1 QCD Jets

QCD two jets production, where one of the jets is able to pass our electron selection requirements because of the fluctuation of particle contents of jets and

statistical nature of shower development, while the other jet can lose energy in the detector cracks or its energy can fluctuate to give a sizable missing $\not{E}_T$ in the calorimeter. Therefore some of them are identified as W events. However, the characteristics of missing $\not{E}_T$ in the QCD events is still different from that in W events. So the missing $\not{E}_T$ spectra are studied in order for us to understand the background and quantify it for our precision measurements.

We begin the study by first selecting a "signal" sample from the data triggered by ELE_HIGH which was also used to trigger our final W and Z data samples. The standard selection requirements for an electron from W, that there be one EM cluster with $E_T > 25GeV$ within the good fiducial volume of the calorimeters, well isolated, small H-matrix χ^2 and good track match, are applied to EM clusters in this sample. The missing $\not{E}_T$ distribution is shown in the upper half of the Figure 4.1. In the distribution, the peak at the low missing $\not{E}_T$ region is mostly due to the di-jet events where one jet happens to be identified as an "electron" and the missing $\not{E}_T$ comes mostly from the energy fluctuation. Another small bump at around 40 GeV which is about half of the mass of the W, corresponds to true signals of $W \rightarrow e\nu$ decays. The di-jet events' contribution to high missing $\not{E}_T$ events is decreasing rapidly as the missing Et becomes bigger. At the low missing $\not{E}_T$ region, however, the W signals' contribution is far less than those from QCD dijet events. Based on this observation, we then can try to reconstruct a missing $\not{E}_T$ distribution from another relatively pure QCD di-jet events sample. By an appropriate normalization of that QCD sample, we can estimate how many tail events of QCD di-dijet origin have extended into our signal region which is defined as the region above 25 GeV in missing $\not{E}_T$. After a number is obtained we can subtract this background from our signal sample.

A correct selection of QCD di-jet sample is thus important for this study. And we have to make sure that in this sample most of W events are appropriately removed. For the purpose of removing the W events from the sample, we ask the isolation parameter to be large to require there be some activities around the "electron". The missing $\not{E}_T$ spectrum will reflect the shape of the QCD jets background because isolation and missing Et are not correlated quantities. We turn to the ELE_MED trigger which is the only EM trigger without isolation cut applied. The ELE_MED trigger events were filtered and events with one electron with $E_T > 25GeV$ satisfying the following cuts were selected,

- Number of calorimeter cells < 20;
- EM fraction > 0.95;
- Isolation > 0.15.

The resulting distribution is shown in the bottom of Figure 4.1. Note that the energy scales of the missing $\not{E}_T$ are corrected for both two samples discussed here.

We then use those two samples to calculate the QCD background in $W \rightarrow e\nu$ data sample. We divide the events into CC and EC according to whether the electron is in CC or EC. This allows us to calculate the cross section for CC electron and EC electron and it can be used as a check to the electron rapidity distribution measurement and consistency of our data sample. The events are further sub-divided into two groups to take into account two different versions of the ELE_HIGH trigger which was used for our W data selection. We call these two groups by their major difference, $EIS = 0.4$ and $EIS = 0.6$. The

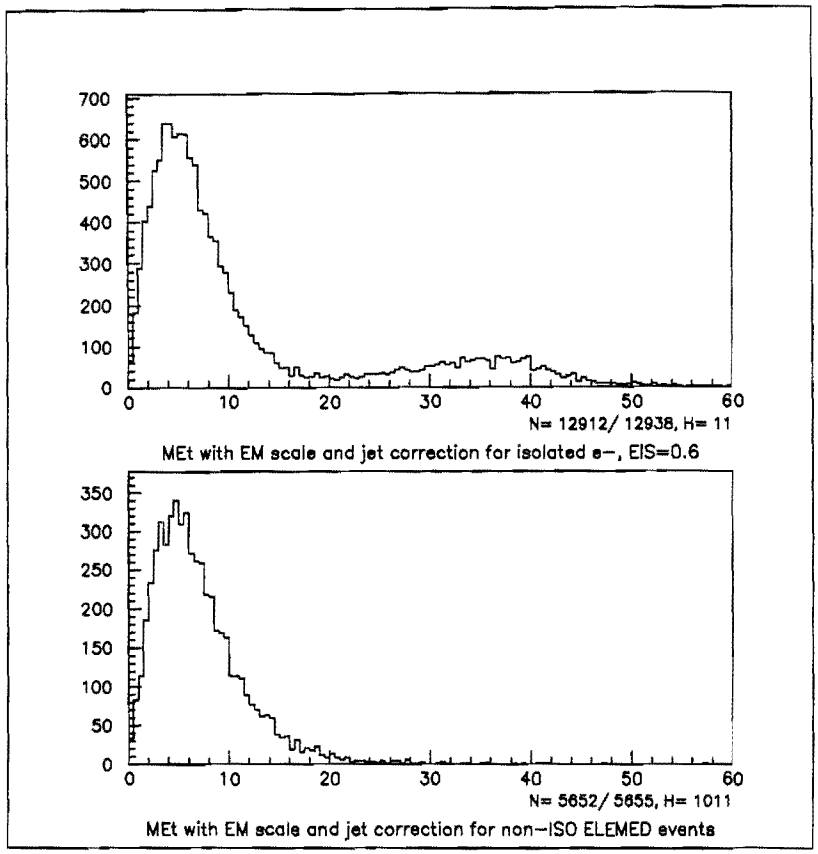

Figure 4.1: The missing $\not\!\!E_T$ distribution. The top plot is for the signal sample, the bottom plot is for QCD background sample.

first one used a cone size of 0.4 to calculate the isolation parameter and the latter used a cone size of 0.6 in the ELE_HIGH trigger. The difference in trigger requirement affects the background because the isolation is devised to reduce the QCD background in the first place.

Using each of these data subsets, we normalize the background sample to the signal sample in the region $0 - 10GeV$ in missing $\not\!\!E_T$ as shown in

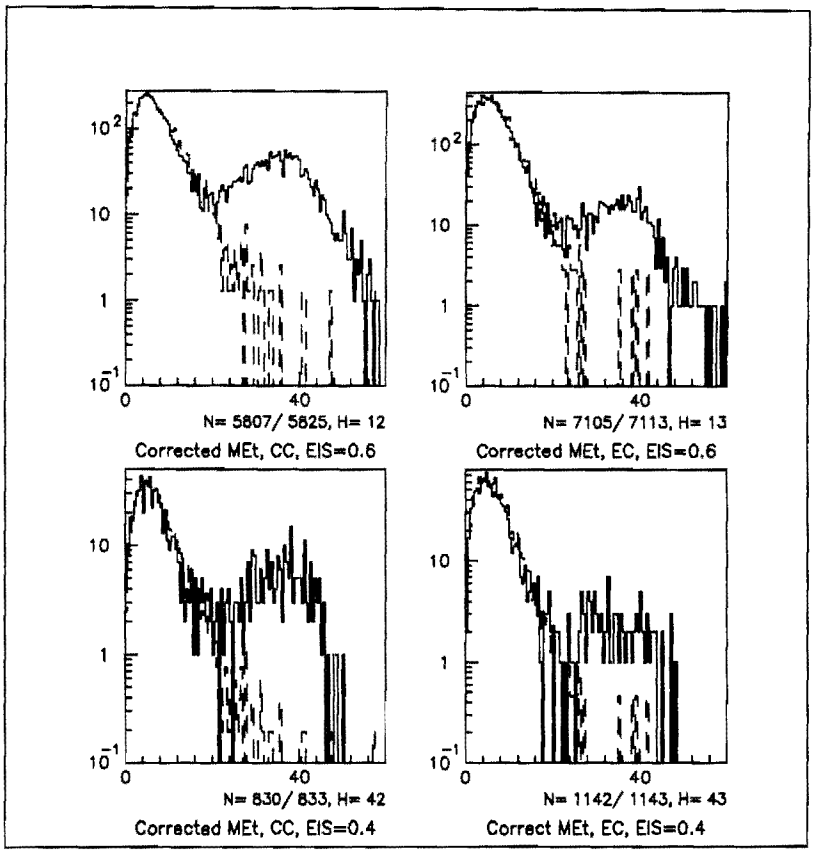

Figure 4.2: The missing $\not\!\!E_T$ distribution. The dotted histograms are QCD background samples normalized in low $\not\!\!E_T$ regions to the signal samples which are shown in solid line.

Figure 4.2. We count the number of events in the background sample with Missing $\not\!\!E_T > 25GeV$ and scale them back to the signal sample. Then we divide the number by the total number of events in our signal sample with missing $\not\!\!E_T > 25$ GeV to obtain the QCD background estimates. All results are shown in table 4.1. For the overall QCD background, we use the relative luminosity and the observed fractions of data in CC and EC to combine all the numbers shown in table 4.1. By using the luminosity, we find that 49.64% of

data used 0.4 cone size and 50.36% used 0.6 cone size in trigger. And then we find 7284 out of 10338 W candidate events have their electrons in CC and 3054 events in EC. Therefore the overall QCD background in our W data sample is

$$f_{QCD} = 3.3 \pm 0.4\%.$$

	CC($EIS = 0.4$)	EC($EIS = 0.4$)
QCD Background(%)	$3.1 \pm 0.5 \pm 0.1$	$4.2 \pm 1.4 \pm 0.2$
	CC($EIS = 0.6$)	EC($EIS = 0.6$)
QCD Background(%)	$2.8 \pm 0.5 \pm 0.1$	$4.0 \pm 1.3 \pm 0.1$

Table 4.1: QCD background in the W sample

4.1.2 $W \rightarrow \tau\nu \rightarrow e\nu\nu$

The process $W \rightarrow \tau\nu \rightarrow e\nu\nu$ is experimentally indistinguishable from the signal events, because in the final states it gives a real electron and all neutrinos contribute to missing $\not{E}_T$. However, since the electron comes from the secondary decay from τ, the P_T distribution of electrons is much softer and no longer has a Jacobian peak at half of the W mass. Instead, it peaks at low P_T region and the spectrum falls off quickly as one goes to high P_T region. This is shown in Figure 4.3. So a 25 GeV cut on P_T of electron will effectively reduce this background to a very low level.

We use the monte carlo to calculate the geometrical and kinematical acceptance A_τ of $W \rightarrow \tau\nu \rightarrow e\nu\nu$ in exactly same way as for the acceptance A_e of $W \rightarrow e\nu$. The detail of the acceptance calculation will be discussed in next chapter. Assuming that the decay rate of $W \rightarrow \tau\nu$ is the same as that

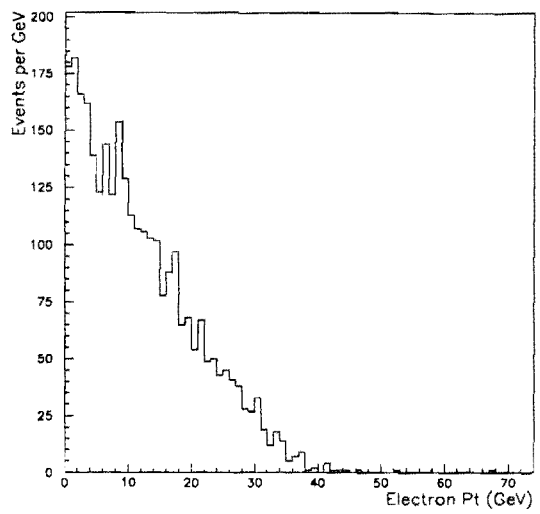

Figure 4.3: P_T distribution of electrons.

of $W \rightarrow e\nu$ and taking the branching ratio for $\tau \rightarrow e\nu\nu$ as 17%, we then can find this background as a percentage of the number of signal $W \rightarrow e\nu$ events by using the formula:

$$f = 17\% \times \frac{A_\tau}{A_e}.$$

The results are:

$$f_{CC} = 1.9 \pm 0.1\%$$

and

$$f_{EC} = 1.9 \pm 0.4\%$$

where f_{CC} is for the events where the electron is found in CC and f_{EC} is for the events where the electron is in EC. By using the numbers shown in Table 5.2, the overall τ background for both CC and EC events is

$$f = 1.9 \pm 0.2\%.$$

The errors are mainly the statistical errors from the MC.

4.1.3 $Z \rightarrow ee$

One of the two electrons from Z decay sometimes goes to the detector crack regions, the energy loss and fluctuation can thus produce a sizable missing $\not{E}_T$ in the event. The final state of one electron and high missing $\not{E}_T$ is the same as that of $W \rightarrow e\nu$. So it is very hard to figure out this fraction directly from the experimental data. In this case a monte carlo simulation is used as well. A full detector simulation (DØ GEANT Monte Carlo [31]) is employed to simulate particle showers in the detector and produce the occasional Z events in which a large fraction of the energy of one of the electrons is lost in the phi cracks in CC or the ICD regions. 10,000 $Z \rightarrow ee$ MC events and 6,000 $W \rightarrow e\nu$ MC events are generated respectively. They are all reconstructed by the same reconstruction programs and the same selection cuts as used for selecting the final W sample in the data are applied. 200 Z events and 1888 W events have survived the cuts. As is shown here, using the W monte carlo sample has advantage of cancelling out the reconstruction efficiencies and reducing the systematics of the monte carlo simulation program. This background as a fraction of pure $W \rightarrow e\nu$ events is then estimated as

$$f = \frac{\sigma(p\bar{p} \rightarrow Z \rightarrow ee)}{\sigma(p\bar{p} \rightarrow W \rightarrow e\nu)} \times \frac{200}{10000} \times \frac{6000}{1888}.$$

If we take $\sigma(p\bar{p} \rightarrow Z \rightarrow ee)/\sigma(p\bar{p} \rightarrow W \rightarrow e\nu)$ as 0.1, which is close to both theoretical calculations and our observed ratio of W and Z productions, then $f = 0.6\%$ is obtained.

The major systematic error sources are the statistical errors of the MC samples, the Missing $\not{E}_T$ correction routine and the error of the cross section

ratio $\sigma(p\bar{p} \rightarrow Z \rightarrow ee)/\sigma(p\bar{p} \rightarrow W \rightarrow e\nu)$. The error from the Missing $\not{E}_T$ correction routine is assigned as the difference between the result with and without the $\not{E}_T$ correction. We vary the cross section ratio from 0.09 to 0.11 to get the error contribution from the ratio. Finally

$$f = 0.6 \pm 0.1\%.$$

4.1.4 $Z \rightarrow \tau\tau$

The process $Z \rightarrow \tau\tau$ has the same rate as $Z \rightarrow ee$, which is already 10 times smaller than the rate of W production. Each electron from τ decay has a similar soft P_T spectrum as discussed in the case of $W \rightarrow \tau\nu$. It is thus obvious that this background is negligible.

4.2 Background in the Z Sample

The background in $Z \rightarrow ee$ mainly consists of Drell-Yan e^+e^- pair production and QCD jets events where jets fake electrons.

4.2.1 QCD Jets

Because the invariant mass distribution of two electrons from the Z decay has a well defined resonance peak, and the spectra for background sources are relatively flat at the resonance peak region, the invariant mass distributions become the major tool we rely on to estimate the backgrounds. The basic idea is to use the theoretical Z/γ line shape and the experimentally determined shape of the QCD background to fit to the data, including the tail region on either side of the Z resonance peak. The absolute normalization of the QCD

background is determined by the fitting and the percentage of the background in the signal sample is hence deduced.

First we'd like to get the invariant mass shape of the QCD backgrounds. The di-jets events are selected from a sample of Jet_Min trigger [32]. The P_T cut for both jets is 25 GeV. The spectrum of mass of two jets is shown in Figure 4.4(a). The rate of a jet faking an electron or a photon and the integrated luminosity of the Z sample are used to normalize the spectrum.

The spectrum is fitted with an exponential function in the mass range 65 - 250 Gev. The fitted function is

$$f_{dijet}(m) = e^{0.7762-0.02367m}.$$

The spectrum of direct-photon plus jets processes is also interesting because those events also can mimic our signal events. A mass spectrum of direct-photon and jets from DØ direct photon group [33] is used. The faking rates of jets to electrons are used to normalize the spectrum. For the spectrum shown in Figure 4.4(b), the fake rate used is 10^{-3} and the integrated luminosity is $14pb^{-1}$.

The mass spectrum is fitted with another exponential function in the same mass range mentioned above. The fitted function is shown below,

$$f_{\gamma jet}(m) = e^{0.7363-0.03448m}.$$

Then a monte carlo generator is used to generate the complete Z/γ line shape. The basics of the generator are described in detail in [34] and the QED radiative corrections are also included in this generator [35]. The main function of this generator here is to add the QED radiation to electrons and also simulate the detector energy resolution. It generates events according to

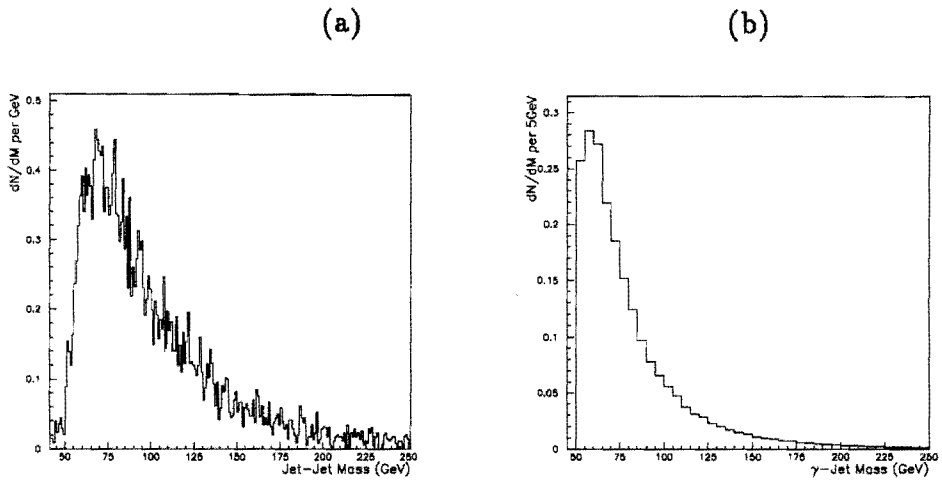

Figure 4.4: Mass spectra for (a) di-jet events (b) γ jet events.

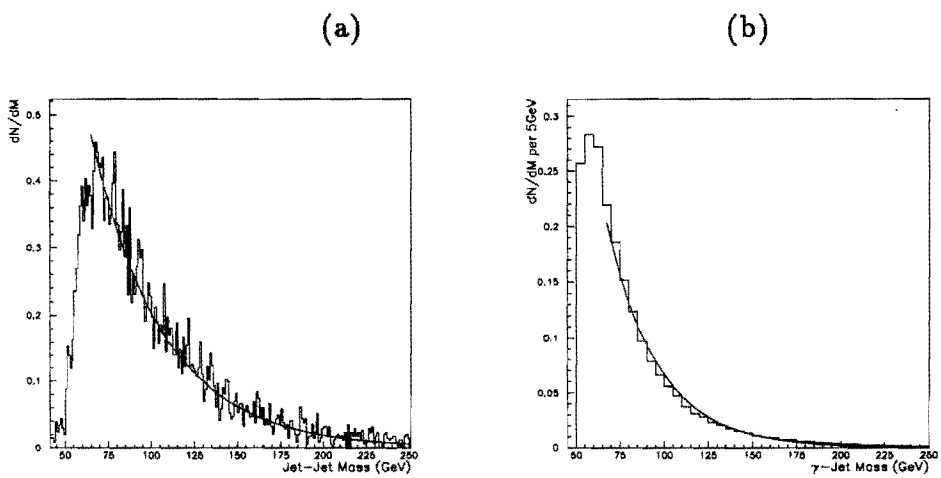

Figure 4.5: Same spectra with the fitting functions superimposed.

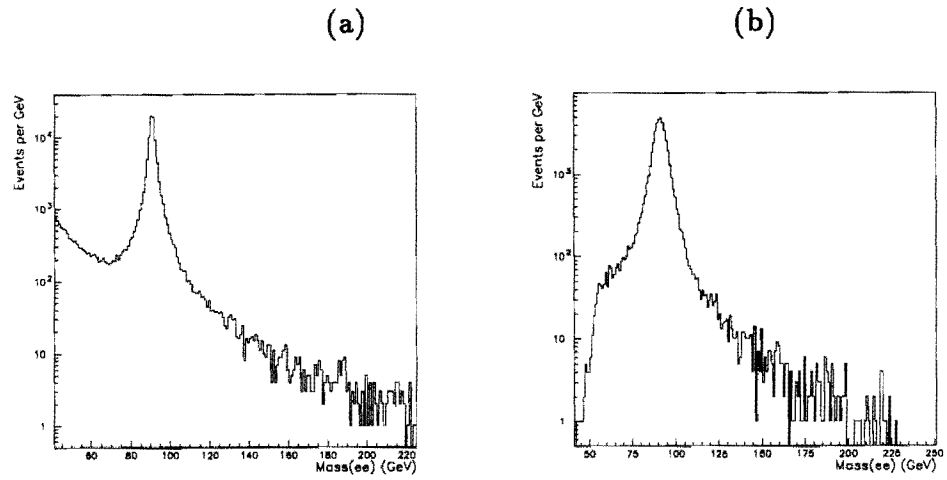

Figure 4.6: (a) The mass distribution used for input; (b) The reconstructed mass distribution.

an input mass distribution as shown in Figure 4.6(a), which is the di-lepton mass spectrum of the process $p\bar{p} \rightarrow Z/\gamma \rightarrow ee$ generated by Pythia monte carlo program [36] which has the full matrix elements calculations. After a Z/γ event is generated, we require that the smeared P_T of both electrons be greater than 25 GeV. If the event satisfied the requirement, the invariant mass is reconstructed. The final mass spectrum of those events is shown in figure 4.6(b). We use $f_z(m)$ to represent this mass spectrum.

The maximum likelihood method is employed to fit the data with our MC spectrum.

We use $f(m)$ to represent the mass spectrum of data. Then

$$f(m) = n_1 \times f_z(m) + n_2 \times f_{background}(m)$$

where n_1 and n_2 are the normalization parameters. They are not independent, however, because the number of the data events is fixed. It is straight-

forward to see that

$$\int f(m)dm = n_1 \times \int f_z(m)dm + n_2 \times \int f_{background}(m)dm.$$

And if we define $N_{data} = \int f(m)dm$, $N_1 = \int f_z(m)dm$ and $N_2 = \int f_{background}(m)dm$, then

$$n_1 = \frac{N_{data} - n_2 \times N_2}{N_1}$$

and

$$f(m) = \frac{N_{data} - n_2 \times N_2}{N_1} \times f_z(m) + n_2 \times f_{background}(m).$$

N_1, N_2 and N_{data} are all known quantities, so there is only one free parameter n_2. The maximum likelihood method is used to fit this parameter.

If we only include dijets contribution in the background, namely $f_{background} = f_{dijet}$, then we get the fitting results which are shown in the section A of table 4.2. The fitting results are 2 to 3 sigma away from $n_2 = 1$ which corresponds to the case that the normalization mentioned earlier in this section is the absolute normalization.

Because in our Z selection we allow the second electron to be either a PELC subject or PPHO subject, the direct γ plus jet events also contribute to the background. So $f_{background} = f_{dijet} + f_{\gamma jet}$. Then the fitting results are shown in the section B of table 4.2. It can be shown that now the fitting results are only 1-2 sigma away from $n_2 = 1$. Note that in both cases, the absolute number of background events in the mass window $75 - 105GeV$ are very similar.

As shown in Figure 4.7(a), the number of events in the low mass tail region fluctuates from bin to bin, this contributes to the fluctuations in the fitting

A. $f_{background} = f_{dijet}$	
Mass fitting range	n_2
$61.2 - 121.2GeV$	3.75 ± 1.00
$71.2 - 121.2GeV$	3.70 ± 1.20
B. $f_{background} = f_{dijet} + f_{\gamma jet}$	
Mass fitting range	n_2
$71.2 - 121.2GeV$	2.75 ± 1.00
$71.2 - 111.2GeV$	2.25 ± 1.06
$75.2 - 121.2GeV$	1.38 ± 1.06
$77.2 - 121.2GeV$	1.75 ± 1.13

Table 4.2: Fitting of n_2

values of n_2 for different mass fitting ranges. For the nominal value, we take the median one and the error of the size of 1.0 is assigned.

$$n_2 = 2.0 \pm 1.0.$$

With this value, the fit of data with Monte Carlo is shown in Figure 4.7(b), and the χ^2 per degree of freedom is about 0.9.

This n_2 value corresponds to $2.8 \pm 1.4\%$ in terms of the percentage of the observed number of events whose masses are within the mass window 75 GeV to 105 GeV.

4.2.2 Drell-Yan Electron Pair Production

The Drell-Yan process $\gamma \rightarrow ee$ produces the exact final state as $Z \rightarrow ee$. Therefore the experimentally observed production of electron pairs should correspond to the square of sum of the amplitudes M_γ and M_Z. However, we are only interested in the term $|M_Z|^2$, so the Drell-Yan fraction $|M_\gamma|^2$ and the interference term should be deducted from our event counting.

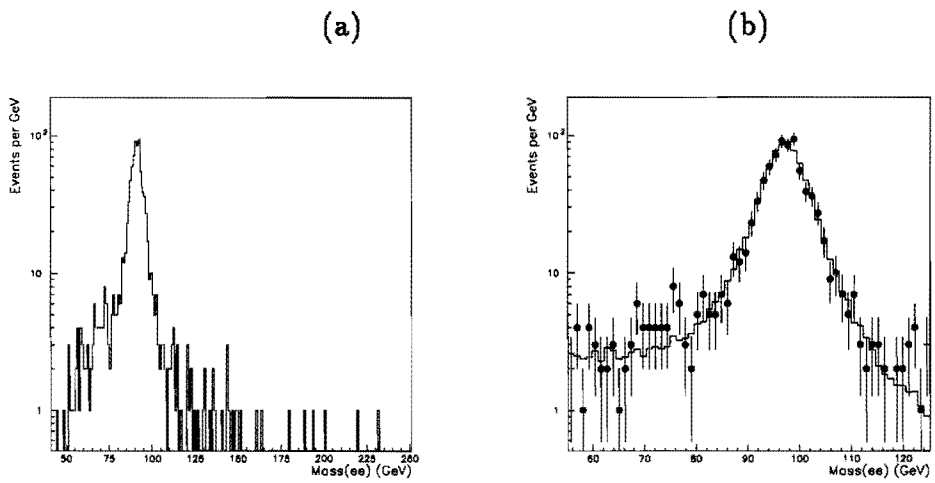

Figure 4.7: (a) The mass distribution of data. (b) Fit data with Monte Carlo with $n_2 = 2.0$. The histogram is Monte Carlo.

We use ISAJET Monte Carlo [37] to estimate those two terms relative to the pure Z production and express them as the fraction of the number of pure Z. The number is found to be 1.35%. We also use another Monte Carlo PYTHIA and find the similar number. This background is thus found to be $1.3 \pm 0.1\%$.

4.2.3 $Z \rightarrow \tau\tau$

The process $Z \rightarrow \tau\tau$ and where both τ decay to electron can be a background to our $Z \rightarrow ee$ sample. 900 monte carlo $Z \rightarrow \tau\tau \rightarrow ee$ events are generated. After 25 Gev P_T cut for both electrons is applied, only 17 events survive. If we further require the mass be greater than 75 Gev, then only 1 event is left. Considering the 17% branching ratio for $\tau \rightarrow e$, this background

can be safely neglected.

Chapter 5

The Acceptance for W and Z

The processes $p\bar{p} \rightarrow W \rightarrow e\nu$ and $p\bar{p} \rightarrow Z \rightarrow ee$ are identified in the experiment by the decay electrons and missing energy created by the escaping neutrinos. But only a fraction of all the events produced at DØ are observed, because the coverage of the detector is not completely 4π in solid angle and it is absolutely necessary to make some cuts to select the interesting events out of the huge background.

The acceptance for W or Z production in the electron channel is defined as a fraction of all the $W \rightarrow e\nu$ or $Z \rightarrow ee$ events produced in $p\bar{p}$ collisions. In this fraction of events, the electrons should go through the good geometrical region of the calorimeter and the transverse momenta of two leptons should satisfy our kinematical cuts.

5.1 Fiducial and Kinematic Region

The good fiducial regions are the parts of the detector where response to electrons is well understood. The selection of the good fiducial regions is based upon the consideration of having as small systematics as possible and also relatively small loss of statistics.

There is no electromagnetic calorimeter coverage around $\eta = \pm 1.3$ at all. The Central Calorimeter and End Calorimeters are also physically located in different cryostats. This naturally divides the whole space into the Central Calorimeter coverage and End Calorimeters coverage. In the Central Calorimeter, we require that $|\eta|$ should be smaller than 1.1 in order to have complete four EM layers coverage. Between every two adjacent EM modules in the CC, there is an EM crack which corresponds to a particular value in ϕ coordinate. The detector response to electrons in those 32 crack regions is not as good as in the middle of the modules. This effect was studied in DØ Test Beam run. It is shown in Figure 5.1 [38] that when an electron with 100GeV energy is about 0.005 radians in ϕ away from the module edge, the energy response is almost uniform and energy loss due to the leakage to the crack is negligibly small. However, we choose to cut 0.01 just to make sure we have the uniform and close to 100% response for electrons with any other large energies. Therefore the good fiducial regions in CC are defined as the areas where $|\eta| < 1.1$ and ϕ to be 0.01 radian away from the 32 crack regions.

The outer radius scan of EM module of the end calorimeter at the DØ Test Beam Run suggested that at the region where $|\eta| < 1.4$, large corrections are needed for electron energies; at the region where $1.4 < |\eta| < 1.5$, the corrections range from 0 to 15% with an uncertainty of the correction to be about

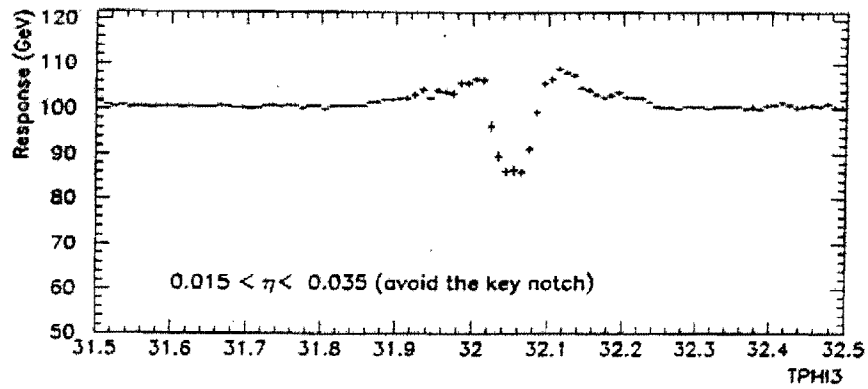

Figure 5.1: Mean response to 100 GeV electrons vs TPHI3 in the vicinity of the module crack, where TPHI3 $= \Phi \times 64./2\pi$ and the crack is at $\Phi = \pi$.

25% [39]. Therefore, in order to reduce the systematic error and complexity of the analysis, we require $|\eta| > 1.5$. Although the EM trigger goes as high as $|\eta| = 3.2$, at the high η region, the trigger efficiencies drop rapidly and the background increases, so we require $|\eta| < 2.5$ as well. The electrons from W and Z events are populated in the central rapidity region, so the event loss due to this cut is very small. Finally the good fiducial regions in the end calorimeters are defined as the areas where $1.5 < |\eta| < 2.5$.

The transverse momentum P_T spectrum of the electrons from W or Z is a continuous spectrum with a Jacobian peak at the half mass of W or Z. Because the Level 2 trigger had already had 20 GeV cut on the electrons, the efficiency of trigger is a turn-on function of the reconstructed electron P_T. We have to make a higher cut on electron P_T in order to reduce the systematic errors caused by the trigger inefficiencies. Thus we determine to choose 25 GeV as the kinematic cut for electrons. The missing $\not{E}_T$ or the neutrino P_T is positively correlated with the electron P_T. We choose 25 GeV for the missing

$\not{E}_T$ as well, without losing many more events, but having one advantage of reducing the QCD background in the W sample.

5.2 Physics and Detector Simulation

A simple monte carlo is used for acceptance evaluation. The parton level physics is generated by one of the physics generators used at DØ . In this generator, $\hat{s}$ or an invariant mass for W or Z is first generated. Then the vector boson decays to leptons in its rest frame. The leptons are boosted to the lab frame by the longitudinal and transverse motions of W or Z. The longitudinal motion is caused by the longitudinal momentum imbalance of quark and antiquarks from proton and antiproton, which is mainly determined by the parton distribution functions and the center of mass of the system. The transverse motion is caused by the QCD radiation of initial partons or higher order α_s W or Z production. A theoretical monte carlo calculation of double differential cross section $d^2\sigma/dP_T d\eta$ for W and Z is used to describe this transverse motion. This W or Z P_T calculation program is originally written by Arnold and Kauffman [40] and has the second-to-leading order precision. It uses standard perturbative method for the high P_T region, resummation scheme for the low P_T region and a matching scheme in between. The procedure for generating a P_T is to first generate the rapidity η for W or Z from the quarks' momentums. Then the double differential cross section is used to generate a P_T at that rapidity value η. After all the four vectors of leptons and vector boson are generated, the differential cross section is calculated and used as a weight for this event. We generate 1,000,000 such events and use the weights to get the acceptance of the geometrical and kinematical cuts we make.

The relevant detector simulation is also included in the monte carlo program. The vertex position of collisions is offset to $z = -8$ cm and generated from a gaussian distribution with a sigma of 30cm to simulate the measured vertex distribution of Run 1a. The energy of electron is smeared with a resolution of

$$(\frac{\sigma}{E})^2 = C^2 + (\frac{S}{\sqrt{E}})^2$$

where $S = 15.7\%\sqrt{GeV}$ for all the calorimeters, C is a constant term and has the values shown in the table 5.1.

	CC	ECN	ECS
Scale	1.072 ± 0.002	1.025 ± 0.005	1.012 ± 0.007
Constant term	0.0212 ± 0.006	0.0316 ± 0.009	0.043 ± 0.01

Table 5.1: EM scale and resolution

The efficiency of L2 P_T cut is folded in by sampling L2 turn-on curves obtained by studying the data from ELE_MEDIUM trigger [41]. Because the ELE_MEDIUM trigger has also a P_T cut of 16 GeV, there seems to be a bias to the efficiency measurement. However, since the turn-on curve approaches the full efficiency very fast as one can see from the figures 5.2 and 5.3, we get the more accurate trigger efficiency as the offline reconstructed P_T cut goes higher. At 25 GeV for offline P_T, the efficiency is about 97% to 98%, the bias error is negligible. The trigger had changed during the course of the DØ run 1a. Some fraction of data used the fast vertex(z) information from the Level 0 to calculate the P_T in Level 2, which had a larger error. The other fraction of data, which was taken in the later part of the Run 1a, used the slow z correction in Level 2 P_T calculation. This affects the accuracy of Level 2 P_T

calculation therefore the efficiency differs. So two sets of acceptance numbers are calculated to incorporate this effect.

The radiative corrections are made as well. We first calculate the acceptance of pure radiative processes $W\gamma$ or $Z\gamma$ where energy of γ has to be greater than 20 MeV. When calculating the acceptance we define a cone centered at the electron with the cone size defined as $R = \sqrt{\delta\eta^2 + \delta\phi^2}$, where $\delta\eta$ or $\delta\phi$ is the difference in η or ϕ between electron and photon. If $R < 0.3$ then we add the energies of both electron and photon together and treat the sum as the electron energy. Otherwise the energy of electron is left intact. Then we use a fraction estimation [42] which says that approximately 35% of W events or 74% of Z events will radiate a γ with energy greater than 20 MeV to combine the acceptances of W/Z and $W/Z\gamma$ to get the final acceptances. The radiative corrections are about 0.6% for W and 1.6% for Z.

For W, the missing $\not{E}_T$ is reconstructed from the P_T of electron and the P_T of W as shown in the following

$$\not{E}_T = \mathbf{P_T^W} - \mathbf{P_T^e}.$$

The electron P_T is smeared as the EM energy. The W P_T is smeared as the hadronic energy, which is about $50\%/\sqrt{E}$, because W P_T is experimentally measured from the recoil jets of the W boson. Since most of these recoil jets are soft, a correction factor of 0.83 [34] is introduced to simulate the mismeasurement of the soft jets at DØ . The numerical factor 0.83 is obtained by studying the balance of P_T sum of two electrons and the soft recoil jets in the Z events. The effect of underlying events is also folded in. A large number of minimum biased events was collected and the missing P_T of those events is reconstructed and added to the above $\not{E}_T$ to simulate the resolution

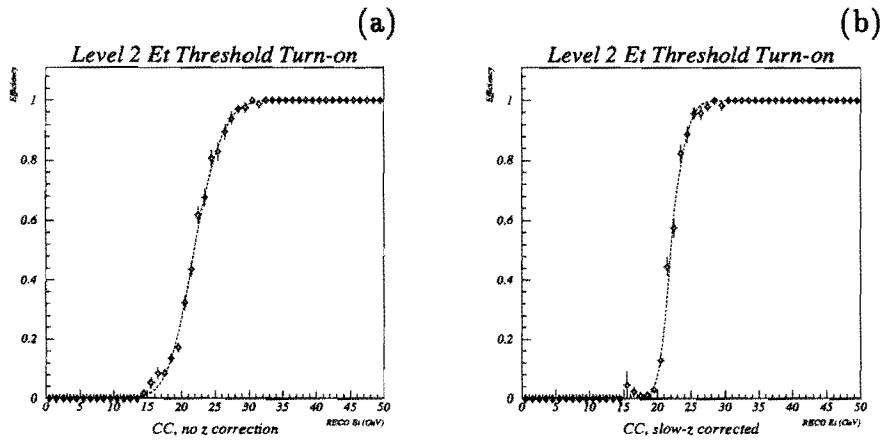

Figure 5.2: Turn-on curves for CC electrons (a) without z correction (b) with z correction. The lines are fitted functions to the data points.

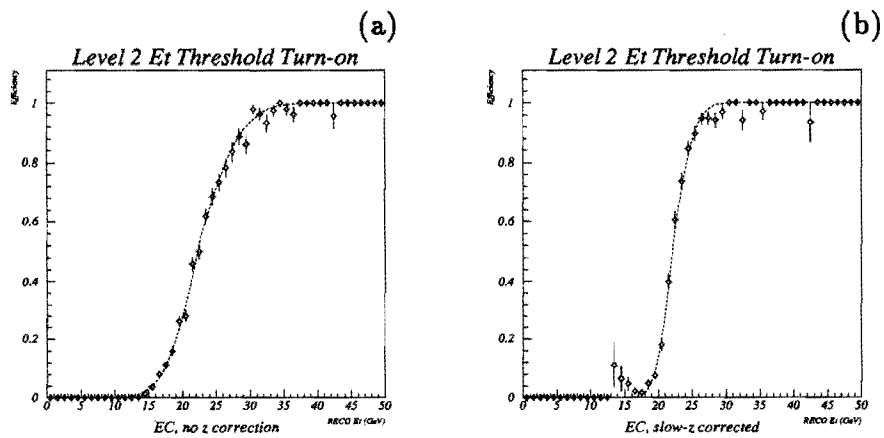

Figure 5.3: Turn-on curves for EC electrons (a) without z correction (b) with z correction. The lines are fitted functions to the data points.

contributed from the underlying event.

For Z, we also require the invariant mass of the lepton pairs be within the mass window from 75 GeV to 105 GeV. The efficiency of this cut is 97.74% by cutting directly on the resolution smeared mass in the Monte Carlo simulation program. However, the program has a mass window from 65 GeV to 115 GeV already, which is to increase the event generating efficiency. A relativistic Breig-Wigner shape is used to calculate the acceptance of this window and it is about 97.70%. So the overall efficiency is 95.5%. The error is estimated by varying the shape which is affected by the structure functions. The resolution effect is studied and the difference between using the smeared mass and unsmeared mass is only about 0.1%.

Finally the acceptance numbers are calculated. For the nominal numbers, the following masses and widths are used.

$$M_W = 80.21\text{Gev}, \Gamma_W = 2.12\text{Gev};$$

$$M_Z = 91.18\text{Gev}, \Gamma_Z = 2.487\text{Gev}$$

where the mass of W is the current world average from the results of UA2, CDF(89), CDF(92) and DØ and the width of W is the world average from the particle data book [19]. The numbers about Z are from the LEP average. The structure function used is CTEQ2PM.

The acceptance for W thereby is

$$A^W = 45.59\%(\text{no z correction})$$

or

$$A^W = 46.12\%(\text{slow z correction}).$$

Then the integrated luminosity is used to combine these two numbers to get the overall acceptance. By comparing the luminosity, the fraction of the data without slow-z correction in the total data sample is found to be 21.58% and the fraction with slow-z correction is 78.42%. Therefore,

$$A^W = 46.01 \pm 0.60\%$$

And for Z

$$A^Z = 36.31 \pm 0.36\%.$$

The difference between the numbers of no z and slow z correction in Z's case is substantially small and is neglected. The errors for both W and Z acceptance are discussed in detail in the next section.

The fractions of W or Z events with electrons in CC or EC are shown in table 5.2. The errors are mostly from the structure function variations.

	CC	EC	
W's	$69.3 \pm 0.5\%$	$30.7 \pm 0.5\%$	
	CC/CC	CC/EC	EC/EC
Z's	49.5 ± 0.5	$40.5 \pm 0.3\%$	$10.0 \pm 0.4\%$

Table 5.2: Fractions of W/Z events with electrons in CC or EC

5.3 Systematics Discussion

Because we use the monte carlo to calculate the acceptance, the errors of the acceptance mainly come from the uncertainties in the monte carlo program.

We summarize the systematic errors for acceptance and the ratio of acceptance in table 5.3. The errors of ratio are assigned independently with the

consideration of the partial cancellation of the systematic errors from A^W and A^Z.

	A^W	A^Z	A^W/A^Z
W/Z P_T spectrum	0.3%	0.2%	0.4%
Structure Function	0.4%	0.6%	0.3%
Radiative Corrections	0.3%	0.4%	0.4%
Turn-on curves	0.3%	< 0.1%	0.3%
Vertex distribution	0.4%	0.4%	0.3%
Electron energy			
resolution	0.1%	0.3%	0.2%
scale	0.3%	0.3%	0.2%
W Mass	0.7%	-	0.7%
W Width	< 0.2%	-	< 0.2%
$\not{E}_T$	0.6%	-	0.6%
Mass cut for Z	-	0.3%	0.3%
Total	1.3%	1.0%	1.3%

Table 5.3: Systematics of Acceptance. A "-" means negligible.

The source for the largest uncertainty of the theoretical P_T spectrum for W/Z is the parameterization of non-perturbative physics at low P_T regime, where QCD resummation method is used. It can be shown that [40]

$$\frac{d\sigma}{dP_T^2 dy} \propto \int d^2b e^{i\mathbf{b}\cdot\mathbf{P_T}} W(b_*) e^{-S_{np}(b)}$$

where b is the impact parameter, conjugate to P_T; W is a complicated function and b_* is basically b itself but is cutoff at b_{max} for the large values of b. $S_{np}(b)$ parameterize the large-b dependence due to non-perturbative physics. In practice, $S_{np}(b)$ can be approximated by

$$S_{np}(b) = b^2[g_1 + g_2 ln(b_{max}Q/2)],$$

and g_1 and g_2 are chosen by fitting to Drell-Yan data. The nominal values are $g_1 = 0.15Gev^2$ and $g_2 = 0.4Gev^2$. We use the set of values $g_1 = 0.09Gev^2$ and $g_2 = 0.25Gev^2$ to determine the variations of the acceptance and assign the variations as the systematic errors from different P_T shapes. We can do so because this set gives $S_{np} = 0.84b^2$ and that is close to the extreme case allowed from fitting the Drell-Yan data. The two sets of g values correspond to two different shapes of the spectrum. However, this change in shape is found out to have only 0.3% effect on the acceptance for W and 0.2% for Z.

The systematics from the structure functions are studied by using 5 sets of structure function: CTEQ2PM, CTEQ2M, CTEQ2MS, GRV, MRSD0' and MRSD-. The acceptance are recalculated for each structure function and the maximum difference is quoted as the systematic error.

The turn-on curve we used is obtained without any cut on the number of vertices. Two other turn-on curves are used to estimate the error, one of them is from the events with only single vertex, the other one with the number of vertices to be greater than one. Because the turn-on efficiency are very high for the W events and even higher for the Z, the error from this source is very small for W and negligible for Z.

The one sigma deviation from the world averaged W mass value is used to estimate the systematics from the uncertainty of mass of W. The acceptance is found to be sensitive to the mass of W. This effect is 0.7% for a change of mass of 0.18 GeV. We change the width from the nominal value by 500Mev and find out that the acceptance is changed by less than 0.2%, therefore it is not sensitive to the W width. For Z the errors from these sources are neglected because the errors on the nominal values are already very small.

The error for simulation of the missing $\not{E}_T$ in an event is mainly from

$\not{E}_T$ smearing and simulation of the energies of soft jets. And the error for scaling the soft jet energy dominates the total error for $\not{E}_T$ simulation. The correction factor of 0.89 which is one sigma away from the nominal value is used to study this systematic. About 0.6% change in acceptance is found and thus assigned as the systematic error from this source.

We vary the sigma of the gaussian distribution of the vertex from 25cm to 35cm. This gives an estimate of error coming from the deviation of the experimental vertex distribution from the one we put in.

The electron energy scale error and resolution also contribute to the systematics of the acceptance. We use the error on the scale correction factors used for correction of the data as shown in table 5.1 to estimate the error from the scale. We also change the constant and the percentage terms in the resolution formula and then compare the acceptance. The errors from both two sources are found to be small.

The radiative correction to the acceptance is dependent on the cone size as shown in last section. Thus the variance of acceptance due to the change of the cone size is used as the major systematic error from this source.

5.4 Comparison of the Monte Carlo with Data

The simulation of the Monte Carlo described in this chapter is checked by comparing several important distributions to those from data. In addition to the detector simulation discussed here, only one number for CC and one number for EC are introduced to simulate efficiencies of the offline cuts. The Monte Carlo samples are normalized to the estimated numbers of W or Z in the data. All plots are shown in Figure 5.4 to Figure 5.7. The Monte Carlo

plots are in histograms and data points are black dots with error bars. One can see the agreements are generally good and some regions with a little excess of data are where the background contributions are expected to appear.

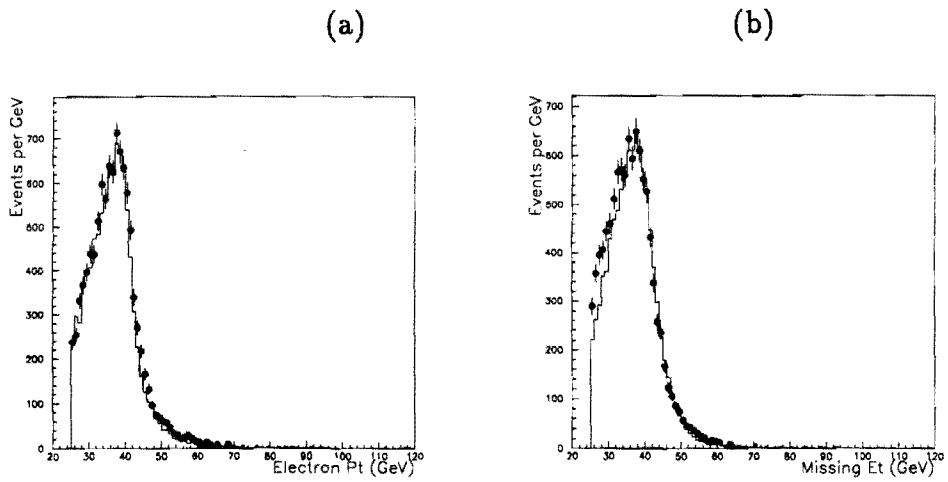

Figure 5.4: For W, (a) P_T of electrons, (b) Missing $\not{E}_T$.

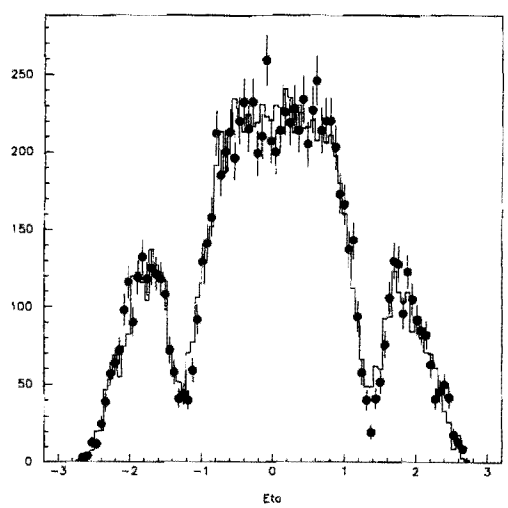

Figure 5.5: η distribution of electrons in the W events.

(a) (b)

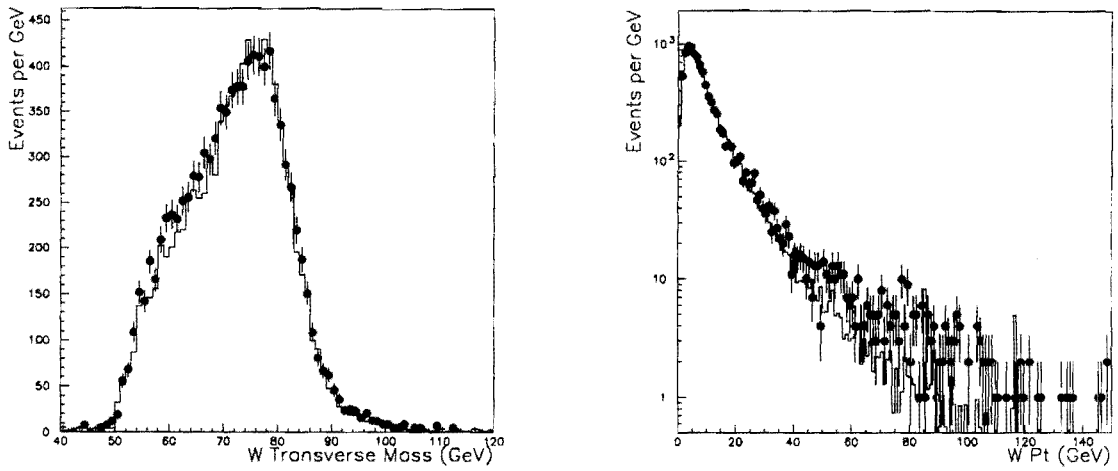

Figure 5.6: (a) W transverse mass (b) P_T of W.

(a) (b)

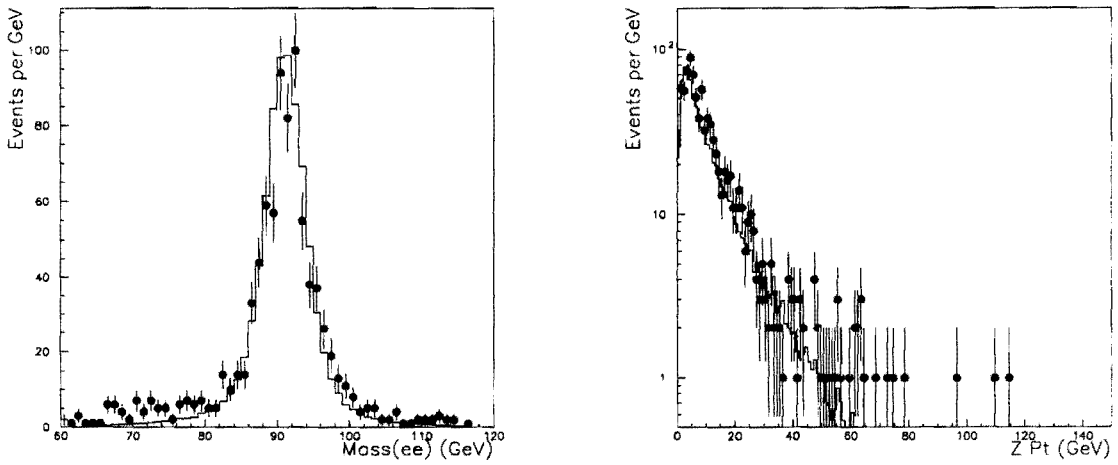

Figure 5.7: (a) Mass of Z (b) P_T of Z.

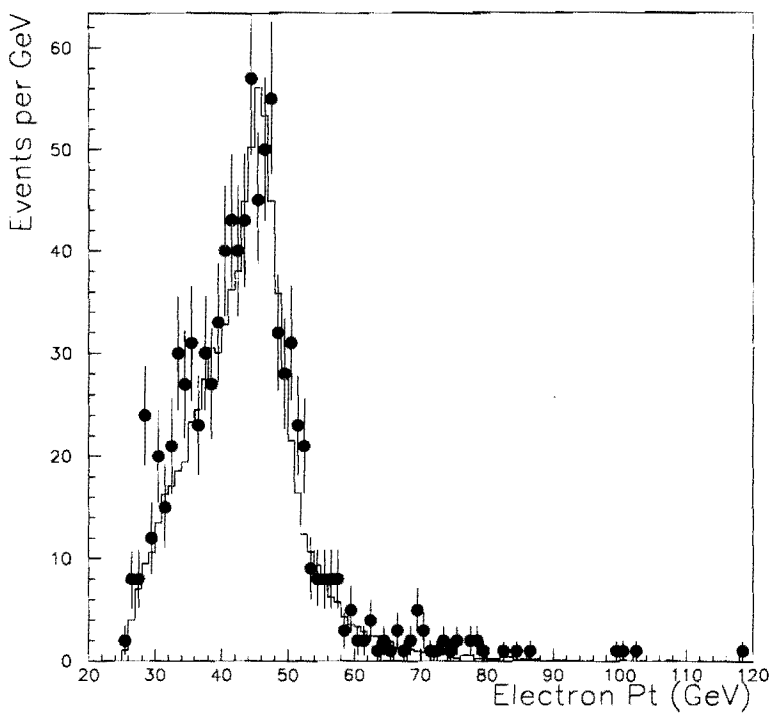

Figure 5.8: P_T of leading electrons in the Z events.

Chapter 6

Efficiency

As we use the trigger and a number of offline selection cuts to select the signals and reduce the background, some fractions of real signals are also lost in this process. The fraction of signals remaining in the sample after a selection cut is made is defined as the efficiency of that particular cut. A good understanding and measurement of the efficiency of all cuts we use is thus very important to our cross section measurements. The efficiencies of the kinematic cuts on the transverse energy or momentum P_T of electron in both trigger level and offline full reconstruction stage have been absorbed into the acceptance calculations. The efficiencies considered to be measured in this chapter are for EM fraction, isolation and H-Matrix χ^2 cuts, which determine the characteristics of showers of particles, and the track in a road requirement as well as the track match quality determination. Also included is the shower shape cuts in the ELE_HIGH trigger.

6.1 Methods

The key to get the accurate measurement of efficiencies of those cuts is to get a clean sample of electrons, which should be selected by another uncorrelated set of cuts, or better yet with as few cuts as possible. An ideal situation would be to shoot pure electron beams into the detector. This was indeed done at DØ test beam when those cuts were first developed and tested. But it is not possible or worthwhile to deliver pure electron beams at actual DØ detector. So we have to rely upon our data to provide the clean electron samples to enable us to measure those efficiencies. Samples like W and Z events themselves are in some sense better than pure electrons because they have all the characteristics of electrons for which we want to measure the efficiencies. Then the next thing to do is to reduce the background in those data samples as much as possible without imposing the cuts of which we want to measure the efficiencies. We have tried using both W data sample and Z data sample. The W sample has good statistics, but since we can't reconstruct the invariant mass of W, we have to rely on some cuts to reduce the background to a low level. The idea is to apply one particular cut and measure the efficiency of other cut assuming the correlation of the two cuts is small. And because the correlation is not well understood, this method is only used to check and confirm our measurement from the Z sample.

Now we turn to the Z sample. In Z events we can reconstruct a well defined Breig-Wigner invariant mass peak. We therefore can put some cuts on one electron and use the mass cut to control the background in the sample, and then use the other electron left in the event as the unbiased electron sample. The only disadvantage here is that this method is limited with the statistics

of the Z data events.

We apply two sets of cuts on one electron of Z separately and use three different background subtraction methods to subtract the background. Therefore 6 measurements of efficiency can be made, and part of systematics is derived from the comparison of these 6 results.

Two sets of cuts are called Standard Tagging cuts and Tight Tagging cuts respectively. They are defined as following,

- Standard Tagging Cuts
  - Tagged PELC passes ELE_HIGH trigger
  - H-Matrix $\chi^2 < 100$ for an electron in CC or 200 in EC
  - $f_{isolation} < 0.15$
  - $f_{EM} > 0.9$
  - $\sigma_{trk} < 10$
- Tight Tagging Cuts
  - Tagged PELC passes ELE_HIGH trigger
  - H-Matrix $\chi^2 < 100$
  - $f_{isolation} < 0.10$
  - $f_{EM} > 0.95$
  - $\sigma_{trk} < 5(10)$ for an electron in CC(EC)

The differences between the results from these two cuts should show how sensitive the efficiency measured by using the second electron of Z would be to the cuts applied to the first electron of Z. The differences are found small, however.

While the electron identification cuts described above are applied to one of two electrons from Z, the second electron is also required to pass some criterion depending upon what cut efficiency we want to measure. The cuts applied to the second electron will be discussed later in this chapter. After two electrons are found in an event, the invariant mass m_{ee} is reconstructed. Then we demand the invariant mass to be within the mass window 86 - 96 GeV for an event to be included in the final sample for efficiency measurement.

The major background in the Z sample is QCD jets productions. The two-body invariant mass distributions are used to study this background. As discussed in Chapter 4, this background can be fitted with exponential functions, or approximated by linear functions in a short range because the indexes of those exponential functions are small. Based on this assertion, three methods of background subtraction are used.

- Method 1: The average of the number of events in the two sideband regions of m_{ee} distribution, $61 < m_{ee} < 71GeV$ and $111 < m_{ee} < 121GeV$, is taken as the background in the signal region.

- Method 2: The mass spectrum of data is fitted to a theoretical function which is the sum of a relativistic Breig-Wigner Z mass shape function convoluted with a gaussian and a linear function. The fitted linear function is used to estimate the number of background events in the signal region as a fraction of the number in the sideband region $60GeV < m_{ee} < 70GeV$.

- Method 3: The same fit in method 2 is used directly to estimate the background. Dual sideband regions $m_{ee} < 70GeV$ and $m_{ee} > 110GeV$ are used to measure the background efficiency in this case.

Then the efficiency of a particular cut is measured by

$$\varepsilon = \frac{\varepsilon_s - \varepsilon_b f_b}{1 - f_b}$$

where ε_s is the efficiency measured by the events in the signal region, ε_b is that measured in the background region and f_b is the fraction of background in the signal region. Note we assume that the events in the background regions are all background. In fact there are actual Z events in those regions too, but that should not change our measurement of efficiency as long as the background events are subtracted from the signals.

6.2 Efficiency for Single Electron Identification

The single electron efficiency can be expressed as

$$\varepsilon = \varepsilon_{trig} \cdot \varepsilon_{RECO} \cdot \varepsilon_{trk} \cdot \varepsilon_{shape},$$

where ε_{RECO} stands for the efficiency of an electron passing the minimal cuts of DØRECO software reconstruction package. For our 25 GeV P_T electrons, Monte carlo studies suggest they are 100% efficient. The ε_{trig} is the efficiency of shower shape requirements in trigger and ε_{shape} is the efficiency of shower shape requirements in offline reconstruction. ε_{trk} is the efficiency of associating a good track with an electron. It contains two pieces, one is the efficiency for finding a track around the electron, another is the efficiency of a cut on a parameter σ_{trk} which determines the quality of match between the track and the shower profile in calorimeters.

First we measure ε_{shape}. The requirement for the second electron of Z is that it should be either a PELC or a PPHO object in good fiducial regions and should have $P_T > 25$ GeV. Then the efficiency of the following cuts are measured

- H-Matrix $\chi^2 < 100$
- $f_{isolation} < 0.10$
- $f_{EM} > 0.95$

The efficiency for electrons in the CC and in the EC are measured separately. Six measurements are made corresponding to six methods discussed above. The central value is taken to be the median value closest to the mean, the systematic error is the combinations of statistical error associated with the central value and the half of the difference of the extreme two of six efficiency measurements. The measured efficiencies are:

$$\varepsilon_{shape_cc} = 0.887 \pm 0.015$$

$$\varepsilon_{shape_ec} = 0.890 \pm 0.024$$

where the systematic errors are dominated by the statistics of the event sample.

Then we measure the efficiency of reconstructing a track associated with the electron. The only difference between a PELC and a PPHO object is that a PELC requires a track in a road centered at electron but a PPHO does not. So this efficiency is measured by taking the ratio of the number of electrons which is reconstructed as PELC and number of electrons reconstructed as either PELC or PPHO. Because there is no apparent reason to believe there

is any visible correlation between tracking system and calorimeter system, in addition to requirements that the second electron be either a PELC or PPHO in good fiducial regions, more cuts are applied to it in order to reduce the background level. Those cuts are:

- to have passed ELE_HIGH trigger;
- to have H-Matrix $\chi^2 < 100$ and
- to have $f_{isolation} < 0.15$.

To increase the statistics, the P_T's of both electrons are reduced to 20 GeV. And the track match quality cut on the first electron is dropped. Then the efficiency is obtained for CC electrons and EC electrons. It is about 87% for CC electrons and 83% for EC electrons.

The trigger shape cuts efficiency and the track match quality cuts efficiency are measured in a similar way as we discussed earlier for efficiencies of calorimeter offline shape cuts [44]. The only difference is that the second electron must be first identified as exclusively PELC instead of either PELC or PPHO.

We combine ε_{trig} and ε_{trk} together as ε_{add}. Then six different values of ε_{add} are obtained from six different methods. The systematic errors are assigned by comparing these results. The dominated error source, though, is still from statistics of the Z events sample.

$$\varepsilon_{add_cc} = 0.830 \pm 0.014$$

$$\varepsilon_{add_ec} = 0.774 \pm 0.024$$

6.3 Efficiency for W Events

The selection cuts for electrons from W events were described in Chapter 3. As one can see, the efficiency of "tight" electrons is just the product of ε_{add} and ε_{shape} which we have already measured. Or

$$\varepsilon^W = \varepsilon_{shape} \cdot \varepsilon_{add}.$$

Therefore the results are

$$\varepsilon^W_{cc} = 0.736 \pm 0.018 \pm 0.004$$

$$\varepsilon^W_{ec} = 0.689 \pm 0.028 \pm 0.008$$

where the first errors are the statistical errors and the second errors are assigned systematic errors.

The numbers for CC electrons and EC electrons are combined to give an overall efficiency by weighting CC and EC with acceptance numbers shown in Table 5.2.

$$\begin{aligned} \varepsilon^W &= f^W_{cc}\,\varepsilon^W_{cc} + f^W_{ec}\,\varepsilon^W_{ec} \\ &= 0.722 \pm 0.016. \end{aligned}$$

A reconstruction program efficiency of 0.993 is also found. After including this, we obtain the efficiency for the W events:

$$\varepsilon^W = 0.7166 \pm 0.0153.$$

6.4 Efficiency for Z Events

There are two electrons in a Z event. One of them is selected exactly in the same way as for the electron for W. So the efficiency should be the same. The second one called a "loose" electron is selected without any tracking requirements and trigger requirement, but with all the other cuts being the same. And in fact the efficiency of selecting loose electrons is just ε_{shape} we have measured in this chapter.

The combined efficiency are separated into three categories: CC-CC events where both electrons are in CC region, CC-EC events where one electron is in CC and another in EC and EC-EC events where both electrons are in EC. The efficiencies can be expressed as

$$\begin{aligned}
\varepsilon_{c-c} &= \varepsilon_{add_cc} \cdot \varepsilon^2_{shape_cc}(2 - \varepsilon_{add_cc}), \\
\varepsilon_{e-e} &= \varepsilon_{add_ec} \cdot \varepsilon^2_{shape_ec}(2 - \varepsilon_{add_ec}), \\
\varepsilon_{c-e} &= (\varepsilon_{add_cc} + \varepsilon_{add_ec} - \varepsilon_{add_cc} \cdot \varepsilon_{add_ec})\varepsilon_{shape_cc} \cdot \varepsilon_{shape_ec}.
\end{aligned}$$

There are two electrons in a Z event, if one electron fails the tight electron cuts, the other one still has chance to pass it, so there is a factor of 2 for the first terms in the first two equations and the second term in the third equation. The last term in all three equations are needed to deduct the overcounting because the tight cuts and loose cuts are not independent. An electron having passed the tight cuts can always pass the loose cuts. This has been illustrated by how we measure the efficiency. In fact we have only measured the efficiency of loose electrons and the efficiency of additional cuts for tight electrons.

The final numbers for efficiencies are thus found to be

$$\varepsilon^Z_{c-c} = 0.764 \pm 0.020 \pm 0.005$$

$$\varepsilon^Z_{e-c} = 0.759 \pm 0.019 \pm 0.013$$

$$\varepsilon^Z_{e-e} = 0.752 \pm 0.031 \pm 0.029$$

where the first errors are statistical from the events sample size and the second errors are for systematics of the methods. The overall efficiency is obtained by weighting using the relative acceptance of CC and EC.

$$\begin{aligned} \varepsilon^Z &= f^W_{cc}\varepsilon^Z_{c-c} + f^Z_{ec}\varepsilon^Z_{e-c} + f^Z_{ee}\varepsilon^Z_{e-e} \\ &= 0.761 \pm 0.014 \end{aligned}$$

where f^Z is the fraction of Z events with the configuration such as CC-CC, CC-EC or EC-EC and they can be found in Table 5.2. Then we add the efficiency of 0.993 for each electron and the final efficiency for the Z events is

$$\varepsilon^Z = 0.7502 \pm 0.0227.$$

6.5 Efficiency Ratio

The primary measurement of the thesis is the cross section ratio measurement. Therefore the efficiency ratio of W to Z is of great interest. It is calculated directly in each of six different methods and the systematic error is assigned independently from ε^W or ε^Z. In this way, the correlation of systematic errors of ε^W and ε^Z can be avoided.

The measured efficiency ratio is then

$$\frac{\varepsilon^Z}{\varepsilon^W} = 1.047 \pm 0.019 \pm 0.006.$$

Chapter 7

The W Width Measurement

7.1 W and Z Cross Sections

The event rate, n, for a process with cross section σ is given by the equation

$$n = L\,\sigma,$$

where L is the luminosity. The cross section can then be calculated from the number of observed events and the integrated luminosity:

$$\sigma = \frac{\int n dt}{\int L dt}$$

or

$$\sigma = \frac{N_{obs}(1 - f_{background})}{A \cdot \varepsilon \cdot \int L dt}.$$

N_{obs} is the number of events in our selected final data sample, $f_{background}$ is the fraction of the sample calculated to come from background, A is the acceptance, and ε is the efficiency for accepted events to reach the final sample. These ingredients to the cross section calculation have been discussed in great

detail in the preceding chapters. $\int Ldt$ is the integrated luminosity of the data sample. The signal candidates in the data sample, the N_{obs} events, are selected from the total number of interactions by a specific trigger. The generally measured luminosity must be corrected for some effects which are specific to this trigger. One major correction, arises because the main accelerator beam passes through the detector. The detector is gated off during the brief interval every 20 μs the beam is near the detector. This "dead time" lowers the effective luminosity and must be corrected for.

7.1.1 Luminosity Determination

While the luminosity may be determined directly from the Tevatron beam parameters, a more precise determination, which can be monitored directly in the experiment, is obtained by recording the event rate for a process with known cross section. The integrated luminosity is then $\int Ldt = N/\sigma$. One process we can use to measure the luminosity is $p\bar{p}$ non-diffractive inelastic scattering. The reaction rate is measured by our lowest level trigger system LØ [23].

For the inelastic cross section, the average of the values measured by the CDF and E710 experiments at Fermilab [45] is used. The reaction rate measured by the LØ system corresponds to a a cross section (the LØ visible cross section)

$$\sigma_{L\emptyset} = 48.2\text{mb}.$$

For the ELE_HIGH trigger used in this analysis, after corrections for experimental dead times, multiple interactions, micro-blanking and losses in the offline reconstruction [46], the integrated luminosity is determined to be

$$\int Ldt = 12.4 \pm 1.5pb^{-1}.$$

The 12% systematic error is conservatively estimated from the uncertainty in the $p\bar{p}$ inelastic cross section, and the systematic errors in the acceptance and efficiency of the LØ detector system.

7.1.2 Cross Section Calculations

Using the backgrounds, efficiencies, and acceptances determined in the preceding chapters, the cross sections for $W \rightarrow e\nu$ and $Z \rightarrow ee$ production may be calculated.

The results are summarized in Table 7.1. Some backgrounds were obtained as fractions of the true (W and Z) signal events; they are converted to fractions of observed events (background plus signal) in the table. The changes affect the $W \rightarrow \tau\nu$ and $Z \rightarrow ee$ backgrounds to the W, and the Drell-Yan background to the Z. The corrections are small.

The calculation of the cross sections is now straightforward.

For the W,

$$\begin{aligned}
\sigma \cdot Br(W \rightarrow e\nu) &= \frac{N^W_{obs}(1 - f^W_{background})}{\varepsilon^W A^W \int Ldt} \\
&= \frac{10338(1 - 0.057)}{0.717 \times 0.460 \times 12.4} \\
&= 2.38 \pm 0.02 \pm 0.06 \pm 0.29(\text{nb}),
\end{aligned}$$

where the first error is statistical, the second one is systematic, and the last results from the 12% uncertainty in the luminosity.

	W	Z
Observed Events	10338	775
Background (%)		
QCD	3.3 ± 0.4	2.8 ± 1.4
$W \rightarrow \tau\nu$	1.8 ± 0.1	-
$Z \rightarrow ee$	0.6 ± 0.1	-
Drell-Yan	-	1.2 ± 0.1
Total	5.7 ± 0.4	4.0 ± 1.4
Acceptance	0.460 ± 0.006	0.363 ± 0.004
A^Z/A^W	0.789 ± 0.010	
Efficiency	0.717 ± 0.015	0.750 ± 0.023
$\varepsilon^Z/\varepsilon^W$	1.047 ± 0.019	

Table 7.1: Summary for event yields, acceptances, efficiencies and backgrounds for W and Z.

For the Z,

$$\begin{aligned}\sigma \cdot Br(Z \rightarrow ee) &= \frac{N^Z_{obs}(1 - f^Z_{background})}{\varepsilon^Z A^Z \int Ldt} \\ &= \frac{775(1 - 0.040)}{0.750 \times 0.363 \times 12.4} \\ &= 0.220 \pm 0.008 \pm 0.008 \pm 0.026(\text{nb}).\end{aligned}$$

As shown in Chapter 1, the values predicted from the order α_s^2 theoretical calculations are $\sigma_W = 22.35nb$ and $\sigma_Z = 6.708nb$. If we use the calculated branching ratio, $B(W \rightarrow e\nu) = (10.84 \pm 0.02)\%$ [16], and $B(Z \rightarrow ee) = (3.367 \pm 0.006)\%$ [19], then $\sigma_W \cdot B(W \rightarrow e\nu) \mid_{theory} = 2.42^{+0.13}_{-0.11}$ nb and $\sigma_Z \cdot B(Z \rightarrow ee) \mid_{theory} = 0.226^{+0.011}_{-0.009}$ nb. The errors in the theoretical calculations include a $2.5 - 4.5\%$ uncertainty from the proton density functions,

approximately 3% from the uncertainty associated with the NLO approximation to the pdf's [47], and $0.2-0.6\%$ due to the error in the measured W mass. Within the total errors, the predicted cross sections are in good agreement with our measured values.

The error in the luminosity measurement should be reduced significantly in the future. Thus good precision will be achieved for cross section measurements. These results may help theorists fine tune their QCD calculations. On the other hand, since the error in the cross section measured in this thesis is dominated by the uncertainty in the luminosity, the measured rate for W production and the theoretical cross section, with a combined error of 5%, may someday serve to normalize other cross section measurements of interest at the $p\bar{p}$ collider.

7.2 Extraction of the W Width

The cross section ratio is

$$\begin{aligned} R &= \frac{N^W_{obs}(1-f^W_{background})}{N^Z_{obs}(1-f^Z_{background})} \times \frac{\varepsilon^Z}{\varepsilon^W} \times \frac{A^Z}{A^W} \\ &= 10.82 \pm 0.41(stat) \pm 0.29(sys). \end{aligned}$$

Note that the dependence on the luminosity is completely canceled in the ratio. The first error is the statistical error and the second one is the systematic error. Some systematic uncertainties also cancel in the ratio. This ratio R is given by the equation discussed in Chapter 1:

$$R = \frac{\sigma(p\bar{p} \to W)\Gamma(W \to e\nu)\Gamma(Z)}{\sigma(p\bar{p} \to Z)\Gamma(Z \to ee)\Gamma(W)}.$$

Using the theoretical calculation of $\sigma_W/\sigma_Z = 3.33 \pm 0.03$ discussed in Chapter 1 and the world average of the measured values of $\Gamma(Z \to ee) = 0.08384 \pm 0.00027 GeV$ [19], and $\Gamma(Z) = 2.490 \pm 0.007 GeV$ [19], the branching ratio is directly obtained,

$$\begin{aligned}\frac{\Gamma(W \to e\nu)}{\Gamma(W)} &= \frac{\sigma(p\bar{p} \to Z)}{\sigma(p\bar{p} \to W)} \times \frac{\Gamma(Z \to ee)}{\Gamma(Z)} \times \frac{1}{R} \\ &= 10.94 \pm 0.41(stat) \pm 0.29(sys) \pm 0.11(other)\%.\end{aligned}$$

The last error comes from the theoretical errors and the errors on the world average values quoted in the above paragraph.

Using the theoretical calculation of the W partial width $\Gamma(W \to e\nu) = 0.2252 \pm 0.0015 GeV$ calculated in Section 1.3, we obtain the W width:

$$\Gamma(W) = \frac{\sigma(p\bar{p} \to W)}{\sigma(p\bar{p} \to Z)} \times \frac{\Gamma(Z)}{\Gamma(Z \to ee)} \times \frac{\Gamma(W \to e\nu)}{R}.$$

Before we substitute numbers, we need to take into account the anticorrelation of the errors due to M_W in the cross section ratio σ_W/σ_Z and the W leptonic partial width. Therefore we study the product $\sigma_W/\sigma_Z \times \Gamma(W \to e\nu)$ as a function of M_W and assign a new systematic error due to M_W. This is combined with the errors from other sources. The final result is

$$\frac{\sigma(p\bar{p} \to W)}{\sigma(p\bar{p} \to Z)} \times \Gamma(W \to e\nu) = 0.7499 \pm 0.0056 GeV.$$

For comparison, the error without consideration of the correlation would be $0.0084 GeV$.

It is now straightforward to extract the W width,

$$
\begin{aligned}
\Gamma(W) &= \frac{\sigma(p\bar{p} \to W)}{\sigma(p\bar{p} \to Z)} \times \Gamma(W \to e\nu) \times \frac{\Gamma(Z)}{\Gamma(Z \to ee)} \times \frac{1}{R} \\
&= 2.058 \pm 0.078 \pm 0.055 \pm 0.018 GeV \\
&= 2.058 \pm 0.097 GeV.
\end{aligned}
$$

It agrees well with the prediction of the Standard Model, $\Gamma(W) = 2.077 \pm 0.014 GeV$ [16], and the current world average, $\Gamma(W) = 2.08 \pm 0.07 GeV$ [19].

Chapter 8

Conclusion

8.1 The DØ Measured W Width

The cross sections for the processes $p\bar{p} \rightarrow W \rightarrow \mu\nu$ and $p\bar{p} \rightarrow Z \rightarrow \mu\mu$ have also been measured at DØ [48]. We can combine the R measurements in the electron and muon channels together to reduce the statistical and systematic errors.

The value of R measured in this thesis is

$$R_e = 10.82 \pm 0.41(stat) \pm 0.29(sys).$$

The R from the muon channel, measured also in this experiment [48], is:

$$R_\mu = 11.8^{+1.8}_{-1.4}(stat) \pm 1.1(sys)$$

where the asymmetric statistical error is caused by the low statistics of Z events in the μ channel.

The error of each measurement is then used as a weight in the combination

of the results. The combined result is

$$R = 10.90 \pm 0.49.$$

The calculation of the branching ratio is the same as in the previous chapter,

$$\begin{aligned}
\frac{\Gamma(W \to e\nu)}{\Gamma(W)} &= \frac{\sigma(p\bar{p} \to Z)}{\sigma(p\bar{p} \to W)} \times \frac{\Gamma(Z \to ee)}{\Gamma(Z)} \times \frac{1}{R} \\
&= 0.1102 \pm 0.0049(stat) \pm 0.0011(sys) \\
&= 0.1102 \pm 0.0050.
\end{aligned}$$

This is in good agreement with the Standard Model calculation of the branching ratio $B(W \to e\nu) = (10.84 \pm 0.02)\%$ for $m_t > M_W$.

The branching ratio $\Gamma(W \to e\nu)/\Gamma(W)$, is largely independent of the W mass and may be used to probe possible new decay modes of the W. Particularly if a lighter-than-W non-Standard-Model top quark were to exist, as this possibility has not been completely ruled out for some non-standard models, a lower limit on the top quark mass can be set. This limit is derived without any knowledge of how the top decays and therefore is independent of the decay modes of the top quark. Since our experimentally measured central value of $\Gamma(W)/\Gamma(W \to e\nu)$ (the inverse of the branching ratio) falls below the Standard Model predicted mean, as shown in Figure 8.1, we use the asymmetric method to calculate the 95% confidence level limit. This means we only use one end of the Gaussian distribution instead of both ends to calculate the probability. Then from the Figure 8.1, we conclude that if the non-Standard-Model top

quark exists, the limit for its mass should be $m_{top} > 61 Gev/c^2$ at the 95% confidence level.

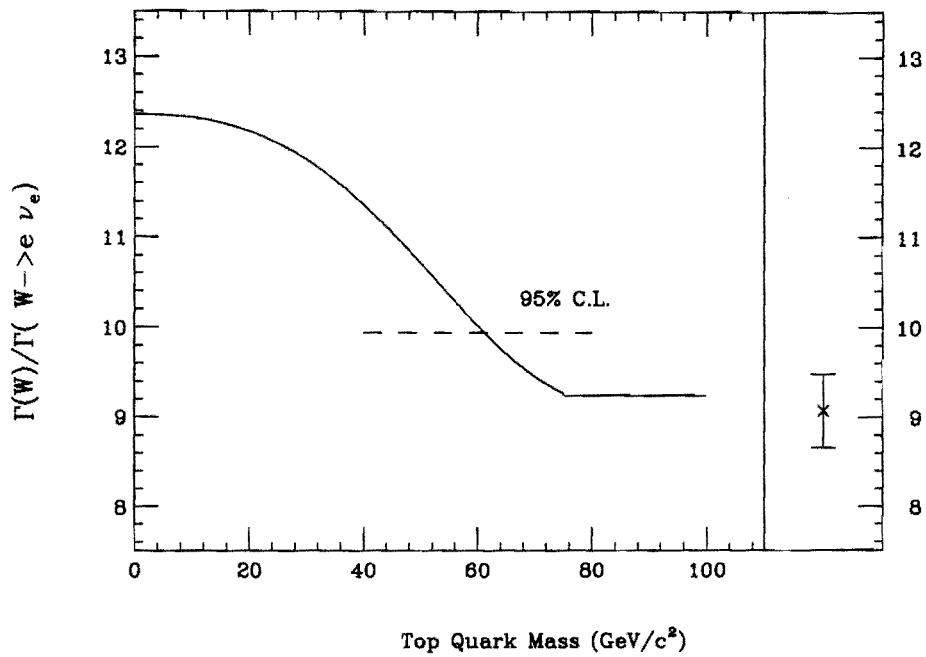

Figure 8.1: Ratio $\Gamma(W)/\Gamma(W \to e\nu)$ as a function of top quark mass. Our data point is shown in the right window.

Also using the method described in the previous chapter, we get the W width:

$$\begin{aligned}
\Gamma(W) &= \frac{\sigma(p\bar{p} \to W)}{\sigma(p\bar{p} \to Z)} \times \frac{\Gamma(Z)}{\Gamma(Z \to ee)} \times \frac{\Gamma(W \to e\nu)}{R} \\
&= 2.044 \pm 0.091 \pm 0.017 GeV \\
&= 2.044 \pm 0.093 GeV.
\end{aligned}$$

This is in good agreement with the Standard Model prediction of

$$\Gamma(W) = 2.077 \pm 0.014 GeV.$$

Using our measured value and the Standard Model prediction, we can set an upper limit on the contribution of unexpected decays to the W width. At 95% confidence level, the limit is $162 MeV$.

8.2 Future Perspectives

The W width has been measured in this thesis to 4.5%. The statistical error is a little larger than the systematic error. Some parts of the systematic error, such as the error due to efficiencies, are caused by statistics also, and the statistics is mainly limited by the number of Z events. Therefore both statistical and systematic errors should be reduced when more data are accumulated. By the end of the second collider run Run-1b at DØ , about $100 pb^{-1}$ of data will be collected, and the total error will be reduced to about 2%.

A direct precise measurement of the W width is possible too when more data are available. Suppose partons i and j with squared center-of-mass energy $\hat{s}$ collide to form either a real or a virtual W, which decays to $l\nu$. The cross section can be expressed as [16]

$$\frac{d\sigma}{d\hat{s}} = \text{const} \times \frac{\Gamma_{ij}\Gamma_{l\nu}}{(\hat{s} - M_W^2)^2 + M_W^2\Gamma_{tot}^2},$$

where Γ_{ij} is the decay width for W into ij and $\Gamma_{l\nu}$ for W into $l\nu$, while Γ_{tot} is the W total width. The integral over $\hat{s}$ is proportional to $\Gamma_{ij}\Gamma_{l\nu}/\Gamma_{tot}$. When $\hat{s}$ is far greater than M_W^2, the expression is almost independent of Γ_{tot}^2.

So one can hope to get enough high $\hat{s}$ events and use it to normalize the total cross section, thus make an absolute measurement of the total W width.

Future experiments at CERN have also the capability to measure the mass and width of W through the process $e^+e^- \to W^+W^-$. With high statistics and good energy scale calibration in a relatively clean background, very high precision measurements are possible.

All these measurements such as the branching ratio and the W width will enable us to examine the electroweak theories more profoundly by being able to test the radiative effects. Various "new" physics which enter into the theory and give measurable radiative effects can be probed by these precise measurements as well. As the current low limit for the mass of the supersymmetry particle wino $\tilde{W}$ is at $45GeV$ [49], exotic decays like $W \to \tilde{W}\tilde{\gamma}$ are still allowed theoretically. Therefore to obtain highly precise measurements of these important physical quantities is still worth pursuing.

Bibliography

[1] S. Weinberg, Phys. Rev. Lett. **19** 1264(1967); A. Salam, Elementary Particle Theory, ed. N. Svartholm(Stockholm: Almqvist,1968), p.367; S.L. Glashow, Nucl. Phys. **22** 579(1961).

[2] F.J. Hasert, et al., Phys. Lett. **46B** 138(1973); Nucl. Phys. **B73**, 1(1974).

[3] G. Arnison, et al., Phys. Lett. **122B** 103(1983); Phys. Lett. **126B** 398(1983); M. Banner, et al., Phys. Lett. **122B** 476(1983); P. Bagnaia, et al., Phys. Lett. **129B** 130(1983).

[4] D.J. Gross, F. Wilczek, Phys. Rev. Lett. **30** 1343(1973); H.D. Politzer, Phys. Rev. Lett. **30** 1346(1973).

[5] Vernon D. Barger, Roger J.N. Phillips, *Collider Physics*, Addison-Wesley Publishing Company, 1987.

[6] Donald H. Perkins, *Introduction to High Energy Physics*, Addison-Wesley Publishing Company, 1987.

[7] The LEP collaborations ALEPH, DELPHI, L3, OPAL and the LEP Electroweak Working Group, Updated Parameters of the Z^0 Resonance

from Combined Preliminary Data of the LEP Experiments, 26 Aug 1993 CERN-PPE/93-157.

[8] R. Hamberg, W.L. van Neerven and T. Matsuura, Nucl. Phys. **B359**, 343 (1991).

[9] K. Hikasa, Phys. Rev. **D29** 1939(1984).

[10] E.L. Berger, F. Halzen, C.S. Kim. S. Willenbrock, Phys. Rev. **D40**, 83(1989).

[11] H.L. Lai et al., MSU-HEP-41024, CTEQ-404, 1994(submitted to Phys.Rev.)

[12] A.D. Martin, R.G. Roberts and W.J. Stirling, Phys. Lett. **B306**, 145(1993); **B309**, 492(E)(1993).

[13] M. Glück, E. Reya and A. Vogt, Z. Phys. **C53**, 651(1992).

[14] We use the world average of $M_W = 80.23 \pm 0.18 GeV/c^2$ from DØ Note 2115/CDF Note2552, unpublished.

[15] A. Sirlin, Phys.Rev **D22** 971(1980); W.J. Marciano, A. Sirlin, Phys.Rev **D22** 2695(1980).

[16] J.L. Rosner, M.P. Worah, T. Takeuchi, Phys. Rev. **B49**, 1363(1994).

[17] A. Denner, Fortschr. Phys. **41**, 307(1993).

[18] D. Albert, W.J. Marciano, D. Wyler, Z. Parsa, Nucl.Phys. **B166** 460(1980).

[19] The Particle Data Group, Phys.Rev. **D50**, 1174(1994).

[20] DØ Collaboration, S. Abachi et al., Phys. Rev. Lett. **74**, 2632(1995); CDF Collaboration, F. Abe et al., Phys. Rev. Lett. **74**, 2626(1995).

[21] W.S.Hou, E.B. Tsai, C.Q. Geng, P. Turcotte, preprint NTUTH-94-15/NHCU-HEP-94-16.

[22] N. Cabbibo, in *Proceedings of the Third Workshop on Proton-Antiproton Collider Physics*, Rome, 12-14 January 1983, edited by C. Bacci and G. Salvini(CERN,Geneva,1983),p.567.

[23] DØ Collaboration, S. Abachi *et al.*, Nucl. Instrum. Methods **A338**, 185(1994).

[24] G. Barbellini, *Calorimeter in Particle Physics*, CERN Preprint, CERN-EP/86-203 (November 28, 1986).

[25] S. Youssef, Computer Physics Communication **45** 423(1987).

[26] M. Narain for DØ Collaboration, *Electron Identification in the DØ Detector*, Preprint, FERMILAB-Conf-93/054-E.

[27] M. Paterno, DØ internal note 1374, March, 1992.

[28] N.J. Hadley, DØ internal note 904, November, 1989.

[29] Q. Zhu, PhD thesis, chapter 7, unpublished.

[30] U. Heintz, DØ internal note 1758, June, 1993.

[31] F. Carminati et al., *GEANT User's Guide*, CERN Program Library, Dec. 1991; J. Womersley, DØ internal note 1520, August, 1992.

[32] Private communication with Geary Eppley.

[33] Private communication with Bob Madden.

[34] Q. Zhu, PhD thesis, Chapter 6, unpublished.

[35] Private communication with John Sculli and Marcel Demarteau.

[36] T. Sjöstrand. Computer Physics Commun. **82**, 74(1994).

[37] F. Page, S.D. Propopopescu, *ISAJET Monte Carlo*, BNL 38034(1986).

[38] W.G.D. Dharmaratna, Terry Heuring, DØ internal note 1577, Dec. 1992.

[39] Private email communication with Tony Spadafora.

[40] Peter B. Arnold, Russel P. Kauffman, Nucl. Phys. **B349**, 381(1991); Peter B. Arnold, M. Hall Reno, Nucl. Phys. **B319**, 37(1989).

[41] Private communication with Peter Grudberg.

[42] Private communication with Allen Mincer.

[43] Qiang Zhu, PhD thesis, chapter 6, unpublished.

[44] P. Grudberg, DØ internal note 2316, Oct. 1994.

[45] N. Amos, J. Bantly, A. Brandt, R. Demina, A. Goldscmidt, J. Linnemann, R. Partridge, L. Paterno, D. Puseljic, J. Thompson, DØ internal note 2186, June 1994; J. Bantly, R. Plunkett, S. Pruss, M. Tartaglia, DØ internal note 2318, Oct. 1994.

[46] N. Amos, J. Linnemann, R. Partridge, L. Paterno, etc., DØ internal note 2031, Jan. 1994.

[47] W. L. van Neerven and E. B. Zijlstra, Nucl. Phys. **B382**, 11(1992).

[48] C. E. Gerber, PhD thesis, unpublished.

[49] V. Barger, R. W. Robinett, W. Y. Keung, R.J. N. Phillips, Phys. Rev. **D28**, 2912(1983); Lepton-Proton High Energy Physics Conference(LP-HEP 91), Geneva, 1991.